Developing alkali-activated controlled low-strength material (CLSM) using urban waste glass and red mud for sustainable construction

Xiao, Rui; Nie, Qingke; Dai, Xiaodi; Wan, Zhi; Zhong, Jingtao; Ma, Yuetan; Huang, Baoshan

DOI
10.1016/j.jobe.2024.111202

Publication date
2024

Document Version
Final published version

Published in
Journal of Building Engineering

Citation (APA)
Xiao, R., Nie, Q., Dai, X., Wan, Z., Zhong, J., Ma, Y., & Huang, B. (2024). Developing alkali-activated controlled low-strength material (CLSM) using urban waste glass and red mud for sustainable construction. *Journal of Building Engineering*, *98*, Article 111202. https://doi.org/10.1016/j.jobe.2024.111202

Journal of Building Engineering 98 (2024) 111202

Contents lists available at ScienceDirect

Journal of Building Engineering

journal homepage: www.elsevier.com/locate/jobe

Developing alkali-activated controlled low-strength material (CLSM) using urban waste glass and red mud for sustainable construction

Rui Xiao [a,b,*], Qingke Nie [c], Xiaodi Dai [d,**], Zhi Wan [e], Jingtao Zhong [f], Yuetan Ma [g], Baoshan Huang [f]

[a] Department of Civil and Environmental Engineering, University of California, Los Angeles, CA, USA
[b] Department of Material Science and Engineering, The University of Tennessee, Knoxville, TN, USA
[c] China Hebei Construction & Geotechnical Investigation Group Ltd., Shijiazhuang, 050227, China
[d] Magnel-Vandepitte Laboratory, Department of Structural Engineering and Building Materials, Ghent University, Ghent, Belgium
[e] Microlab, Faculty of Civil Engineering and Geosciences, Delft University of Technology, Delft, the Netherlands
[f] Department of Civil and Environmental Engineering, The University of Tennessee, Knoxville, TN, USA
[g] School of Traffic and Transportation Engineering, Changsha University of Science and Technology, Changsha, 410114, China

ARTICLE INFO

Keywords:
Controlled low strength material (CLSM)
Alkali-activated material (AAM)
Red mud
Bauxite residue
Waste glass powder
Glass cullet
Toxicity characteristic leaching procedure (TCLP)

ABSTRACT

Using industrial waste in controlled low-strength material (CLSM) offers many benefits and addresses waste management issues. However, identifying optimal CLSM design while balancing environmental impacts and engineering properties poses a notable challenge. Herein, new alkali-activated CLSM formulations based on urban waste glass and red mud (RM) are proposed for the first time with systematic investigations into the material properties and sustainability. The formulations involve the ternary blends of slag, glass powder (GP) and RM as the binders and crushed glass as aggregate. Our observations show RM has a clay-like texture with complex crystalline phases rich in Al and Fe. Increasing the proportion of RM to GP notably decreases the flowability, extends the setting time and impairs the mechanical properties. Nevertheless, red mud demonstrates a crucial role of reducing bleeding level especially for the mixtures with high proportions of glass aggregate. The standard leachate tests as per toxicity characteristic leaching procedure (TCLP) show the heavy metals leached from the CLSM are below the concentration limits and exhibit low mobility. The microstructural and thermodynamic analyses reveal the precipitation of calcium-(sodium-)aluminosilicate hydrate (C-(N-)A-S-H) as the major binding material. The reactive Fe and Al in red mud most probably contribute to the formation of hydrogarnet phases. Moreover, the suggested CLSM formations typically exhibit reduced carbon emissions and lower costs compared to the traditional CLSM produced with cement and fly ash, underlining their environmental sustainability and cost-effectiveness. This study provides a potential guideline for the flowable fill construction in the regions with bauxite producers.

---

* Corresponding author.Department of Civil and Environmental Engineering, University of California, Los Angeles, CA, USA
** Corresponding author.
E-mail addresses: r.xiao@ucla.edu (R. Xiao), x.dai@imperial.ac.uk (X. Dai).

https://doi.org/10.1016/j.jobe.2024.111202
Received 3 May 2024; Received in revised form 10 September 2024; Accepted 29 October 2024

Table 1
Advantages of using CLSM in construction applications.

Advantages of CLSMs	Description	References
Ease of placement	The self-compacting and flowable attribute of CLSM simplifies the placement process, reducing the need for extensive compaction efforts.	[1,63]
Labor savings, time efficiency and cost-effectiveness	The self-leveling properties of CLSM minimize the need for manual labor during placement, contributing to reduced labor requirements, construction timeline and cost.	[1,64]
Improved soil stabilization and reduced settlement	CLSM can enhance soil stability when used as backfill. It provides support to underground structures, reduces settlement, and helps prevent soil erosion.	[65,66]
Consistent material properties	CLSM can be engineered with consistent material properties, ensuring uniformity and reliability in civil engineering applications.	[67]
Reduced environmental impact	The use of CLSM minimizes the need for excessive excavation and replacement of soil, reducing the environmental impact associated with traditional backfill methods.	[5]
Adaptable mix designs	The mix designs can be tailored to meet specific project requirements, allowing for flexibility in engineering applications.	[1,3]
Waste utilization and sustainable construction	Incorporating fly ash and other possible waste into CLSM mixtures contributes to waste utilization and sustainable and environmentally friendly construction practices.	[1,11];

1. Introduction

Controlled low strength materials (CLSM), originally defined by the American Concrete Institute (ACI) Committee 229, have evolved into a group of versatile and functional construction materials with many alternative terminologies: controlled density fill, unshrinkable fill, flowable fill, flowable mortar, soil-cement slurry, plastic soil-cement, K-Krete and various other names [1–3]. The typical material properties for CLSM include the highly flowable, easily pumpable, self-compacting and self-leveling characteristics, and it is engineered to have a low compressive strength (less than 8.3 MPa), making it suitable for various applications where high strength is not a critical requirement [1,4]. In fact, the majority of present CLSM applications usually mandate compressive strengths of 2.1 MPa or even lower. This reduced strength criterion is essential to favor potential future excavation of CLSM [5,6]. In general, CLSM is widely used as a backfill material in utility trenches and around structures because the high flowability makes it easy to fill voids and irregular spaces [1,7]. Its applications also involve embedding utility pipes and even filling abandoned underground structures (i.e., tunnels, tanks etc.) [8]. Table 1 summarizes the advantages of using CLSM in construction applications.

The typical formulations of CLSM involve a mix of several key ingredients (i.e., 8–20 wt% cement, 20–50 wt% fly ash, 20–40 wt% water, 30–60 wt% fine aggregate and chemical admixtures) to obtain the desired properties, while specific formulations can vary significantly based on different construction requirements [9]. To facilitate the utilization and sustainable disposal of waste, the outcomes of recent studies appear to justify industrial byproducts or waste from various industrial processes, depending on the physical and chemical properties, may be suitable for preparing and/or modifying CLSM [1,10]. However, when incorporating industrial waste into CLSM, it is crucial to implement thorough testing and assessment to ensure that the resulting mixture meets the required engineering specifications [11,12]. The proportions of industrial waste should be carefully managed and controlled to achieve the required performances in terms of workability, strength and durability ([11]; Siddique. 2009). In general, both the binders and aggregate can be potentially replaced by waste materials. For example, Kuo et al. [13] formulated CLSM by substituting 20 % of Portland cement with fly ash as the binder and incorporating waste oyster shell sand as the aggregate which effectively enhanced the resistance to sulfate attack. Naganathan et al. [4] investigated the CLSM prepared by cement, quarry dust and industrial waste incineration bottom ash. The results showed quarry dust decreased the water required for constant flow consistency and improved mechanical properties. Wu et al. [14] proposed integrating solid waste from paper mills into CLSM in which fly ash served as a replacement for cement, bottom ash was introduced by partially substituting fine aggregate, and paper sludge functioned as a fibrous admixture.

In recent years, the clinker-free alkali-activated material (AAM) (or sometimes called geopolymer) has been investigated as the sustainable alternative biner which can possibly replace the energy-intensive Portland cement [15–17]. The process of synthesizing AAM generally entails the alkali-activation of aluminosilicate precursor materials, typically sourced from industrial byproducts [18]. The commonly utilized raw materials include class C and class F fly ash, slag and metakaolin. In recent years, more materials such as waste glass, red mud, palm oil fuel ash, natural pozzolan, etc. have also been investigated [19–23]. AAM has demonstrated superior durability properties and comparable compressive strength when compared to ordinary Portland cement (OPC) [18,24,25].

The development of AAM appears to show its potential application in CLSM for enhanced environmental friendliness and waste utilization. In this study, we propose a new OPC-free and cost-effective formulation of CLSM using alkali-activated ternary blends of ground granulated blast-furnace slag, waste glass powder and red mud as the binding material. In the formulation, red mud, increasingly referred to as bauxite residue, is an industrial waste produced in the processing of bauxite into alumina through the Bayer process [26]. The glass powder was produced by crushing urban waste glass which has long been listed as a common municipal solid waste (MSW) [27]. Natural fine aggregate in the CLSM is replaced by crushed waste glass cullet. The specific effects of each ingredient on the engineering properties of CLSM are systematically discussed. The reasons for selecting these three precursor materials are threefold: (1) the hydration of blast-furnace slag as the high calcium precursor is known to facilitate the hardening of AAM at ambient temperature, which is essential to CLSM [28]; (2) urban waste glass, regardless of its source, has a stable chemical composition (~70 % amorphous SiO_2), and the incorporation of 0–50 % glass powder into alkali-activated slag does not significantly impair the compressive strength [29]; [30]; (3) The improper disposal of these three materials poses a huge threat to environment. Typically, the

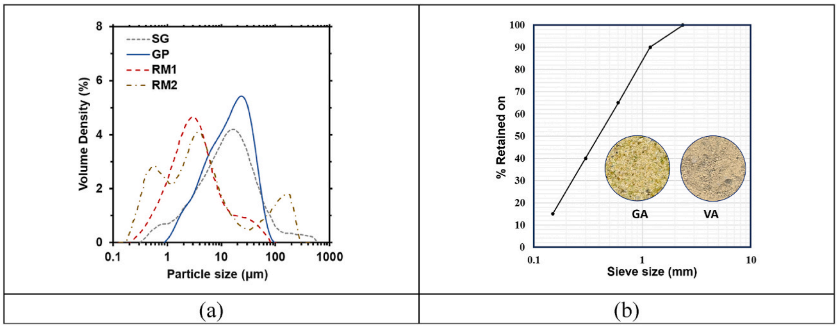

(a) (b)

Fig. 1. (a) Particle size distributions of the raw materials and (b) gradation of fine aggregate.

Table 2
Oxide compositions of SG, GP, RM1 and RM2 by XRF.

Oxide components	SG		GP		RM1		RM2	
	Wt.%	SD	Wt.%	SD	Wt.%	SD	Wt.%	SD
Na_2O	0.041	0.002	5.828	0.340	7.585	0.214	2.890	0.160
MgO	6.424	0.380	0.988	0.085	0.247	0.048	1.560	0.085
Al_2O_3	8.296	0.334	2.087	0.083	23.839	0.414	20.423	0.307
SiO_2	29.190	1.077	74.589	0.723	26.871	1.453	19.000	0.742
P_2O_5	0.044	0.002	0.055	0.023	0.570	0.007	0.288	0.003
SO_3	2.446	0.048	0.360	0.005	0.625	0.004	1.350	0.020
K_2O	0.425	0.014	0.438	0.018	0.075	0.004	0.990	0.015
CaO	51.239	1.004	14.468	0.333	1.678	0.009	21.083	0.064
TiO_2	0.687	0.019	0.104	0.004	7.010	0.101	4.679	0.033
Cr_2O_3	0.007	<0.001	0.003	<0.001	0.176	0.005	0.062	0.001
Mn_2O_3	0.224	0.009	0.018	<0.001	0.315	0.009	0.050	0.002
Fe_2O_3	0.762	0.030	0.946	0.030	30.840	0.777	27.379	0.286
ZnO	–	–	0.004	<0.001	0.012	0.001	0.003	<0.001
SrO	0.065	0.003	0.062	0.002	0.045	0.002	0.151	<0.001

Note: SD = standard deviation.

value-added large-scale utilization of red mud is still a big challenge due to its alkaline nature and the presence of various chemicals. Therefore, this study can potentially contribute to the waste management and the production of environmentally friendly CLSM for sustainable construction.

2. Materials and experimental procedures

2.1. Materials

The cement-free alkali-activated CLSM mixtures were prepared using four industrial byproducts and waste: ground granulated bast-furnace slag (SG), crushed glass powder (GP) and red mud (RM) from two different sources (labeled as RM1 and RM2). The SG, RM1 and RM2 were sourced from China (i.e., Leijiang Co., Ltd. in Hebei, Xinfa Group in Shandong and Xinkuangyuan Co., Ltd. in Guizhou, respectively). The GP was produced by crushing local waste glass containers using a ball mill, and the detailed procedures are described in our previous studies [29,31]. Sine the majority of glass commodities worldwide are made of soda-lime glass, the chemical composition of GP is fairly stable according to previous studies [19,20]. A commercial sodium hydroxide in pellet form (purity >98 %, Fisher Scientific) was dissolved in Milli-Q water to make NaOH solution as the alkaline activator. Two types of fine aggregate were used in this study including crushed glass aggregate (GA) and virgin aggregate (VA). Fig. 1(a–b) illustrate the particle size distributions of all the raw materials and the gradation of fine aggregate.

Table 2 summarizes the oxide compositions of the four materials determined by X-ray fluorescence (XRF). Both RM1 and RM2 are rich in Al_2O_3 and Fe_2O_3, which is different from other common byproducts used in cementitious materials. The results also indicate that red mud sourced from different places may have very different chemical compositions. Fig. 2(a–h) depict the microstructure and mineralogical compositions of the raw materials by scanning electron microscopy (SEM), X-ray diffraction (XRD) and thermogravimetric analysis (TG). The detailed experimental procedures are described in section 2.3. Based on the SEM micrographs, smooth surfaces could be found in GP, and both GP and SG particles showed irregular shapes (Fig. 2a–d). RM1 and RM2 appeared to have much finer particles. The XRD patterns of GP and SG showed the presence of amorphous phase (indicated by the diffuse peak) which is responsible for the hydration and hardening upon alkali-activation [17,32] (Fig. 2e). Some typical minor phases such as calcite, quartz, gehlenite etc. were also found in SG. By careful examinations, the XRD patterns of RM1 and RM2 exhibited much more complicated Al_2O_3- and Fe_2O_3-rich crystalline phases such as boehmite, corundum and hematite (Fig. 2f). Also, the results suggested that RM

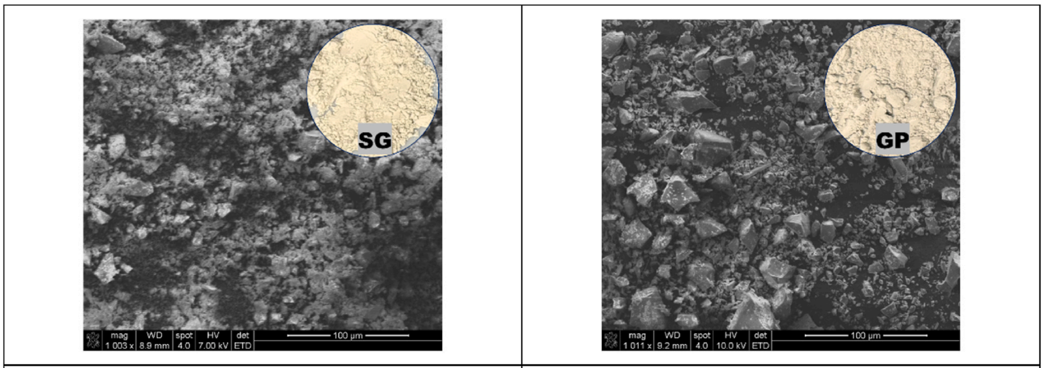

(a) SG

(b) GP

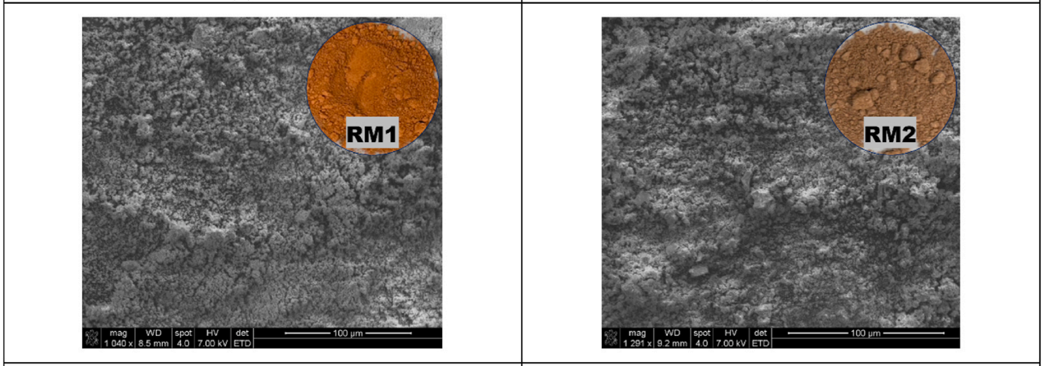

(c) RM1

(d) RM2

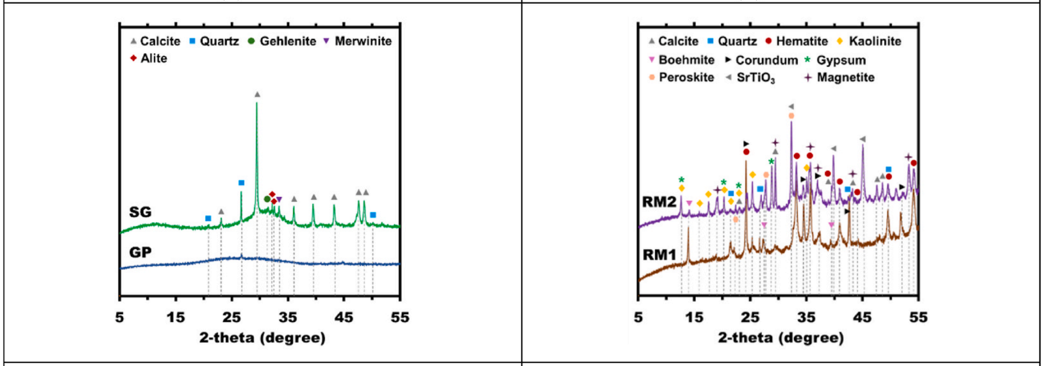

(e) SG & GP

(f) RM1 & RM2

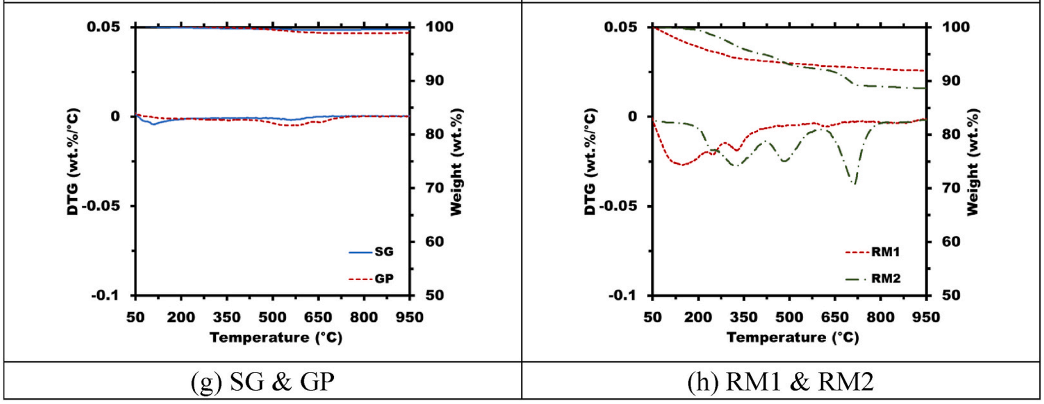

(g) SG & GP

(h) RM1 & RM2

Fig. 2. SEM micrographs, XRD patterns and TG analyses of the raw materials (SG, GP, RM1 and RM2.

Table 3
Formulations of the CLSM. RM1 incorporated mixtures are shown in the shaded area. The water-to-binder ratio was adjusted by the flow consistency requirements for CLSM.

Mix No.	SG: GP: RM (by mass)	Precursor mass percentage in the solid components (%)				VA: GA (by mass)	Aggregate mass percentage (%)		Water-to-binder ratio[a]
		SG + Na_2O	GP	RM1	RM2		VA	GA	
1	40 %: 60 %: 0 %	13.2	17.5	–	–	100 %: 0 %	69.2	–	0.65
2	40 %: 60 %: 0 %	13.2	17.5	–	–	50 %: 50 %	34.6	34.6	0.65
3	40 %: 60 %: 0 %	13.2	17.5	–	–	0 %: 100 %	–	69.2	0.65
4	40 %: 48 %: 12 %	13.2	14.0	3.5	–	100 %: 0 %	69.2	–	0.75
5	40 %: 48 %: 12 %	13.2	14.0	3.5	–	50 %: 50 %	34.6	34.6	0.75
6	40 %: 48 %: 12 %	13.2	14.0	3.5	–	0 %: 100 %	–	69.2	0.75
7	40 %: 48 %: 12 %	13.2	14.0	–	3.5	100 %: 0 %	69.2	–	0.7
8	40 %: 48 %: 12 %	13.2	14.0	–	3.5	50 %: 50 %	34.6	34.6	0.7
9	40 %: 48 %: 12 %	13.2	14.0	–	3.5	0 %: 100 %	–	69.2	0.75
10	40 %: 36 %: 24 %	13.2	10.5	7.0	–	100 %: 0 %	69.2	–	0.80
11	40 %: 36 %: 24 %	13.2	10.5	7.0	–	50 %: 50 %	34.6	34.6	0.80
12	40 %: 36 %: 24 %	13.2	10.5	7.0	–	0 %: 100 %	–	69.2	0.85
13	40 %: 36 %: 24 %	13.2	10.5	–	7.0	100 %: 0 %	69.2	–	0.75
14	40 %: 36 %: 24 %	13.2	10.5	–	7.0	50 %: 50 %	34.6	34.6	0.75
15	40 %: 36 %: 24 %	13.2	10.5	–	7.0	0 %: 100 %	–	69.2	0.80
16	40 %: 24 %: 36 %	13.2	7.0	10.5	–	100 %: 0 %	69.2	–	0.87
17	40 %: 24 %: 36 %	13.2	7.0	10.5	–	50 %: 50 %	34.6	34.6	0.90
18	40 %: 24 %: 36 %	13.2	7.0	10.5	–	0 %: 100 %	–	69.2	0.90
19	40 %: 24 %: 36 %	13.2	7.0	–	10.5	100 %: 0 %	69.2	–	0.80
20	40 %: 24 %: 36 %	13.2	7.0	–	10.5	50 %: 50 %	34.6	34.6	0.85
21	40 %: 24 %: 36 %	13.2	7.0	–	10.5	0 %: 100 %	–	69.2	0.85
22	40 %: 12 %: 48 %	13.2	3.5	14	–	100 %: 0 %	69.2	–	1.03
23	40 %: 12 %: 48 %	13.2	3.5	14	–	50 %: 50 %	34.6	34.6	1.05
24	40 %: 12 %: 48 %	13.2	3.5	14	–	0 %: 100 %	–	69.2	1.05
25	40 %: 12 %: 48 %	13.2	3.5	–	14	100 %: 0 %	69.2	–	0.92
26	40 %: 12 %: 48 %	13.2	3.5	–	14	50 %: 50 %	34.6	34.6	0.95
27	40 %: 12 %: 48 %	13.2	3.5	–	14	0 %: 100 %	–	69.2	0.95
28	40 %: 0 %: 60 %	13.2	–	17.5	–	100 %: 0 %	69.2	–	1.22
29	40 %: 0 %: 60 %	13.2	–	17.5	–	50 %: 50 %	34.6	34.6	1.25
30	40 %: 0 %: 60 %	13.2	–	17.5	–	0 %: 100 %	–	69.2	1.25
31	40 %: 0 %: 60 %	13.2	–	–	17.5	100 %: 0 %	69.2	–	0.95
32	40 %: 0 %: 60 %	13.2	–	–	17.5	50 %: 50 %	34.6	34.6	0.95
33	40 %: 0 %: 60 %	13.2	–	–	17.5	0 %: 100 %	–	69.2	1.00

[a] The water to binder ratios corresponding to 69.2 % VA were used for the binder assessment.

originating from different locations can exhibit significantly varied mineralogical compositions. In this study, the RM2 had several distinct phases including magnetite, kaolinite, perovskite and $SrTiO_3$. The TG results suggested SG and GP were nearly stable under high temperatures (Fig. 2g). The slight drop of SG between 50 °C and 200 °C might indicate a tiny amount of hydration products (C-(N-)A-S-H) formed due to the reaction between SG and the moisture in the air. By contrast, both RM1 and RM2 underwent decomposition and showed continuous mass loss under high temperatures, indicating the presence of complicated hydrous minerals consistent with the data reported by Wang and Liu [33] (Fig. 2h). The mass loss of RM1 between 50 °C and 200 °C was very similar to the performance of C-S-H in OPC, and the mass losses from 200 °C to 575 °C deserve more careful investigations. The mass loss of RM2 between 650 °C and 800 °C was attributed to the calcite phase which agreed with the sharp calcite peak in the XRD pattern (Fig. 2f).

2.2. *Mixture design*

Table 3 summarizes the formulations of all the CLSM mixtures. Generally, the mixing procedures started with the pre-blending of solid precursor materials and fine aggregate, followed by adding alkaline activator (NaOH solution) and then additional water to adjust workability. A Hobart mixer was employed for the mixing compliant to ASTM C305 standard. To be specific, the ternary blends of SG, GP and RM1 (or RM2) were activated by 5 % Na_2O (by total mass of the precursors) to form the binders. This step was achieved by adding NaOH solution to the blends while the equivalent Na_2O content was strictly controlled. The binder-to-aggregate mass ratio was controlled at 1 : 2.25 in this study. The water-to-binder mass ratio was adjusted by adding additional water to different mixtures to meet the high flow consistency requirements for CLSM (i.e., 200 mm in terms of the ACI 299). Here, different water contents were used considering flowability should be prioritized, although a higher water-to-binder ratio may imply a lower compressive strength of the mixture.

2.3. *Experimental procedures*

Following the mixing stage, the flowability of the fresh CLSM was promptly assessed through the flow consistency test in accordance with ASTM D6103. A standard steel cylinder for the test measuring 150 mm in height and 75 mm in inner diameter was filled with fresh CLSM specimens and positioned on level ground. Subsequently, the cylinder was elevated in a vertical direction, and the resulting spread diameter of the CLSM was measured and recorded as its flowability (mm). Incrementally increased water-to-binder ratios were applied to each CLSM specimen until the achieved flowability values reached 200 mm or slightly exceeded this threshold. Afterwards, the selected fresh CLSM specimens were subjected to the tests of bleeding (ASTM C940) and initial setting time (ASTM C430).

The fresh CLSM specimens with the required flowability were cast in 100 mm × 200 mm and 150 mm × 300 mm cylindrical plastic molds, respectively and cured at 25 °C and relative humidity >95 %. Unconfined compressive strength was measured using the 100 mm × 200 mm specimens at 28 d according to ASTM D4832. The 28-d splitting tensile strength was performed on the selected specimens (150 mm × 300 mm cylinders) in terms of ASTM C496/C496M. A constant loading rate of 1.0 MPa/min was applied until failure of specimen. The splitting tensile strength (T) was calculated as Eq. (1).

$$T = \frac{2P}{\pi DL} \tag{1}$$

Where P: maximum applied load (N); D: diameter (mm) of the cylindrical specimen and L: length (mm) of the cylinder.

Slake durability index (SDI) tests were performed as per ASTM D4644 to simulate exposure of the CLSM to nature's continual wetting and drying cycles. After the strength test, the fragments (~50 g) of the CLSM were collected and oven-dried, and the dust was brushed off the fragments. Then, the specimens were soaked in water and rotated in a drum at 20 rpm for 10 min. When the rotation was complete, the fragments were oven-dried again, and this process was repeated for two consecutive cycles. The weight of the specimens retaining on a 2-mm sieve after the whole process was used to characterize the SDI (Eq. (2))

$$SDI = \frac{W_f - C}{W_i - C} \times 100\% \tag{2}$$

Where W_f: mass (g) of drum and oven-dried specimens after rotation; C: mass (g) of drum and W_i: mass (g) of drum and oven-dried specimens before the first cycle.

Leachate test was performed as per toxicity characteristic leaching procedure (TCLP) EPA method to assess the toxic elements coming from the CLSM, simulating the conditions of a landfill by subjecting a waste sample to a series of extraction procedures using an acidic solution. This is done to determine the amount of specific toxic constituents that could potentially leach out of the waste and contaminate groundwater or soil if disposed of in a landfill. The raw materials (SG, GP, RM1 and RM2) and the alkali-activated binding materials (without aggregate) after curing for 28 days were used in the experiment, and the hydrated binders were ground into powder (passing No. 100 sieve). The oven-dried powder specimens were mixed with unbuffered acetic acid solution (pH 2.88 ± 0.05) (solid-to-liquid ratio = 1 : 20) in a beaker which was placed at 25 °C and periodically agitated by a magnetic stirrer for 18 h. Afterwards, the obtained solution was filtered and diluted by 5 % HNO_3. The toxic metals in the diluted solution was tested by Inductively coupled plasma mass spectrometry (ICP-MS). The original concentration was calculated using the dilution factor and the measured ion concentration of the diluted solution. The average value of three test results was taken as the final result.

To analyze the hydration products in the CLSM, the binder in each mixture was subjected to X-ray diffraction (XRD), thermogravimetric (TG) analysis, Fourier-transform infrared spectroscopy (FTIR) and scanning electron microscopy (SEM) with energy dispersive X-ray spectroscopy (EDS) analysis. The XRD was implemented by Empyrean X-ray diffractometer generating Cu Kα X-ray (λ = 1.54 Å) under the working conditions of 40 kV and 40 mA, and each scan (from 5° to 90° (2θ)) took around 30 min to complete. TG was performed using PerkinElmer 400 thermogravimetric analyzer. For each measurement, approximately 30 mg powder specimen was heated from 25 °C to 950 °C in a crucible at a rate of 15 °C/min in the N_2 gas environment. FTIR was conducted by PerkinElmer Frontier, and the spectra from 500 cm^{-1} to 2500 cm^{-1} were collected to assess the evolution of molecular bonds. SEM-EDS was performed using NOVA 230 NanoSEM, and backscattered imaging (BSE) mode was used to analyze the epoxy impregnated bulk CLSM binders after being polished.

2.4. Thermodynamic modeling

In addition to the experiments, Gibbs free energy minimization principle was used to study the phase equilibrium of the reaction process [34]. Typically, the hydration process of AAMs involve the chemical equilibrium between the aqueous and solid phases governed by thermodynamics. GEM-Selektor with PSI/Nagra and CEMDATA 18.01 database was utilized to simulate the hydration of the CLSM binders at 25 °C and one atmospheric pressure across different RM reactivities (0%–30 %) [34]. The reactivities of SG and GP were assumed to be 50 % [29]. The Truesdell-Jones form of the extended Debye-Hückel equation (Eq. (3)) was used to determine the activity coefficients of the aqueous species in the simulation.

$$\log_{10}\gamma_i = -Az_i^2\left(\frac{\sqrt{I}}{1 + Ba_i^o\sqrt{I}}\right) + b_iI \tag{3}$$

In Eq. (3), γ_i and z_i are the activity coefficient and valence of the ion i; I represents the ionic strength of the aqueous phase; A and B are temperature- and pressure-dependent coefficients; $a_i^o = 3.31\text{Å}$ and $b_i = 0.098$ are the semi-empirical ionic-specific parameters to simulate a NaOH-dominated solution.

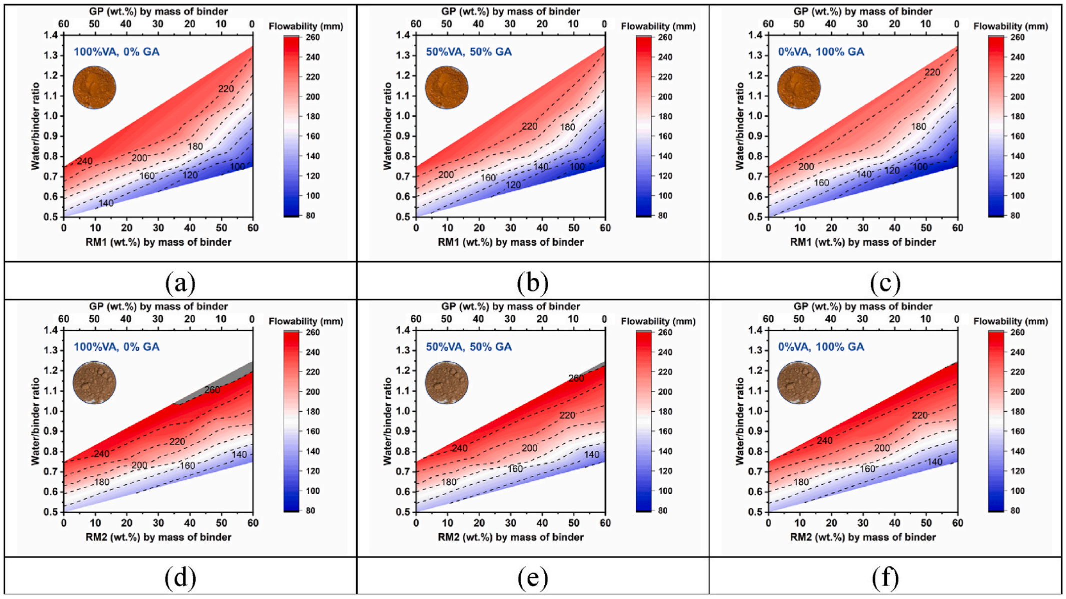

Fig. 3. Flowability values of the fresh CLSM across water/binder mass ratio, RM (wt.%) and GA (wt.%): (a) RM1 mixtures with 0 % GA, (b) RM1 mixtures with 50 % GA, (c) RM1 mixtures with 100 % GA, (d) RM2 mixtures with 0 % GA, (e) RM2 mixtures with 50 % GA and (f) RM2 mixtures with 100 % GA.

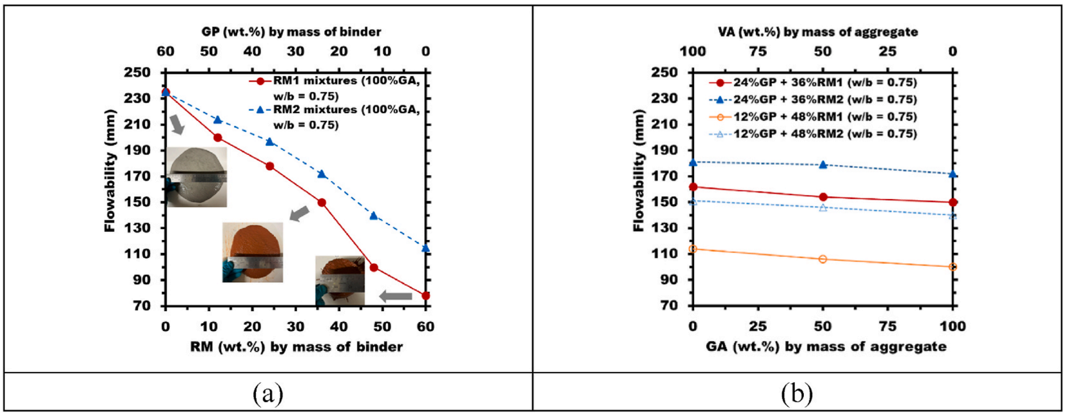

Fig. 4. Effects of (a) RM content and (b) GA content on the flowability of CLSM mixtures at a fixed w/b = 0.75.

3. Results and discussion

3.1. Flow consistency and fresh density

Fig. 3(a–f) depict the flowability results of the fresh CLSM specimens across water-to-binder mass ratio, RM (wt.%) and GA (wt.%). The extensive investigation of flowability was conducted in this study also for the purpose of determining the suitable water-to-binder mass ratio for each mixture (Table 3). For all the RM1 and RM2 mixtures, the measured flowability decreased with increasing dosage of RM (see Fig. 3a–f), indicating the addition of RM was detrimental to the workability of fresh CLSM. This is probably due to the clay-like texture and much smaller particle size of RM (Fig. 1a). The selected mixtures at a fixed w/b = 0.75 were shown as an example in Fig. 4 (a), indicating when the RM weight percentage increased from 0 % to 60 %, the flowability of RM1 and RM2 mixtures decreased from 235 mm to 78 mm and 235 mm–115 mm, respectively. Such a sharp decrease implies more mixing water is needed to achieve the required flowability value (200 mm) for CLSM. In comparison, the influence of the aggregate type was much smaller, and it appears that the incorporation of GA only slightly decreased the flowability (Fig. 4b). In general, the influence of crushed glass aggregate on the workability of cementitious materials is controversial and appears to be related to the aggregate gradation [19,35,36]. This study showed that the fine glass aggregate with the representative size distribution shown in Fig. 1 (b) tended to decrease the workability probably because the irregular surfaces of GA made the materials harder to flow. According to the results (Fig. 3a–f), however, it is

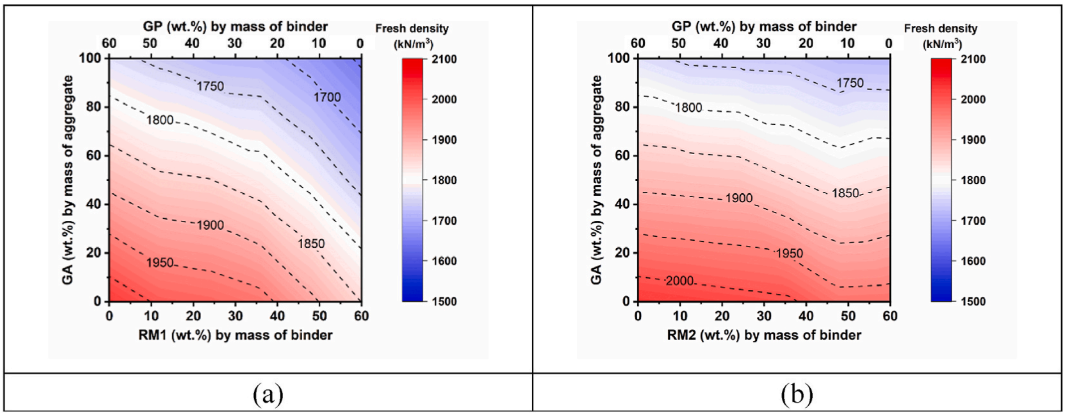

(a) (b)

Fig. 5. Fresh density results of (a) RM1 and (b) RM2 mixtures across the RM (wt.%) by mass of binder and GA (wt.%) by mass of aggregate.

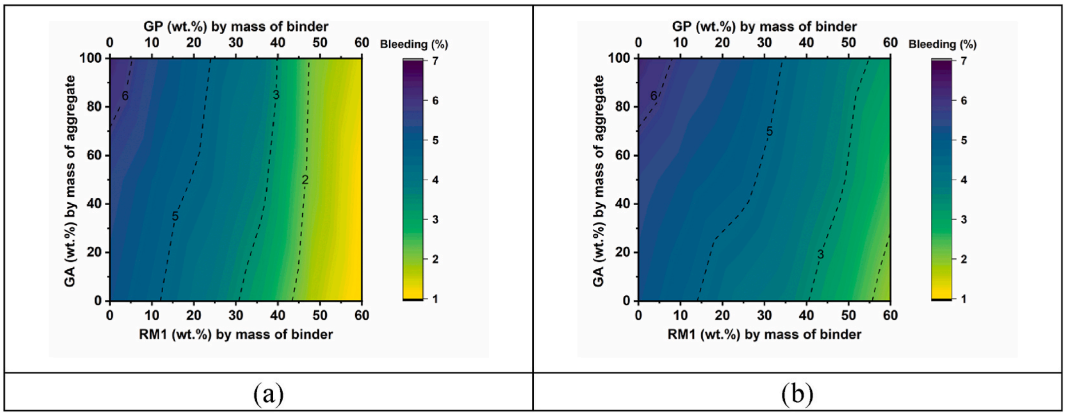

(a) (b)

Fig. 6. Bleeding (%) of (a) RM1 and (b) RM2 mixtures across the RM (wt.%) by mass of binder and GA (wt.%) by mass of aggregate.

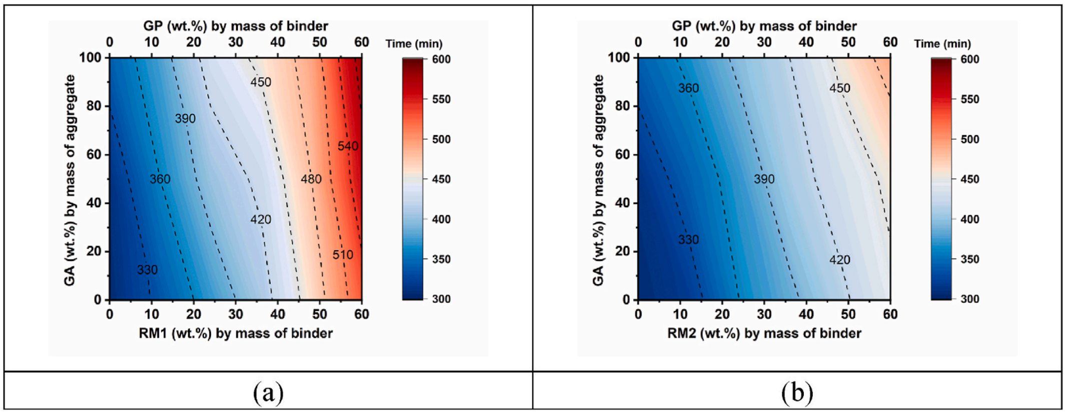

(a) (b)

Fig. 7. Initial setting time of (a) RM1 and (b) RM2 mixtures across the RM (wt.%) by mass of binder and GA (wt.%) by mass of aggregate.

clear that all CLSM formulations could obtain the desirable flowability by adding additional mixing water.

Fig. 5(a–b) show the fresh density results of both RM1 and RM2 mixtures. In general, the fresh density is highly related to the density of each component in the mixture. Since the water-to-binder ratios also varied in the prepared CLSM, the trend of fresh density here is more complicated. As shown in Fig. 5(a–b), the density of both types of mixtures decreased with increasing dosage of RM, and the trend was much more significant for the RM1 specimens. The observed results were mostly attributed to the increasing water-to-binder ratio as the RM content increased, which significantly reduced the fresh density. Also, a decrease in density could be observed as

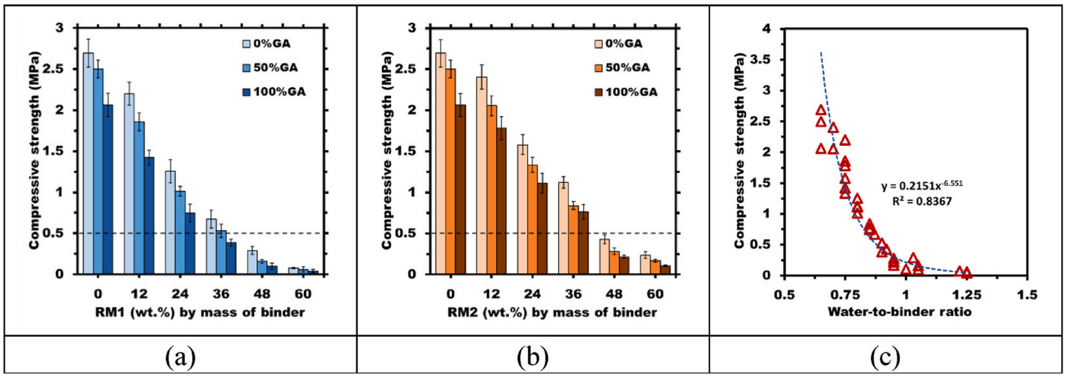

(a) (b) (c)

Fig. 8. 28-d unconfined compressive strength results of (a) RM1 and (b) RM2 mixtures across the RM (wt.%) by mass of binder and GA (wt.%) by mass of aggregate. 0.5 MPa is considered as the lowest strength required for pedestrian traffic. (c) Correlation between unconfined compressive strength and water-to-binder ratio.

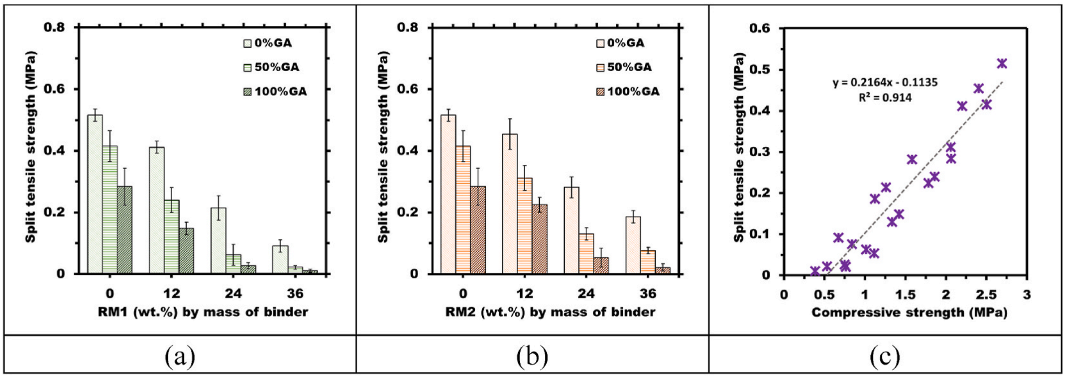

(a) (b) (c)

Fig. 9. 28-d splitting tensile strength results of (a) RM1 and (b) RM2 mixtures across the RM (wt.%) by mass of binder and GA (wt.%) by mass of aggregate. (c) Linear correlation between unconfined compressive strength and splitting tensile strength.

the GA (wt.%) increased, indicating a lower density of GA than that of VA could contribute to a lower fresh density.

3.2. *Bleeding*

Bleeding is quantified as a percentage, calculated by dividing the volume of bleed water (i.e., excessive water released to the top surface) by the initial volume of the CLSM mixture. As shown in Fig. 6(a–b), the bleeding results for all the mixtures ranged from 0 % to 7 % and were sensitive to the CLSM ingredients. Most mixtures achieved a bleeding value smaller than 5 %, which conformed to the bleeding requirements and could be considered as the stable CLSM formulations [5]. According to the results, the bleeding level decreased significantly with increasing RM content. While a larger percentage of GA caused more serious bleeding, the influence was much less significant. It should be noted that the RM-free mixtures were not compliant to the bleeding requirement of CLSM, highlighting the role of both RM contributing to a more stable CLSM mixture during the fresh state.

3.3. *Initial setting time*

Fig. 7(a–b) show the initial setting time of all the CLSM mixtures. Although both RM1 and RM2 contributed to a lower bleeding level, an increasing amount of RM1 or RM2 always led to a more delayed setting based on the results. Previous studies of AAMs suggested that setting time was more related to the calcium content in the binding materials, since calcium compounds have been investigated as the nucleation sites for the hydration products of AAMs [37,38]. In terms of the XRF results, GP, RM1 and RM2 had a CaO content up to 14.468 %, 1.678 % and 21.083 %, respectively (Table 2). Therefore, a higher mass percentage of RM1 over GP definitely resulted in a lower Ca content and hence the longer setting time. Interestingly, the mixture with a higher RM2 content also showed a more delayed setting, although the CaO content increased. The possible reason is that the Ca in RM2 was mostly in the form of crystalline phases (e.g., calcite, perovskite etc.), the function of which was not comparable to that of the Ca in the form of network modifiers in amorphous GP. In addition, it was found that the use of GA also caused a longer setting time, but again, the influence of aggregate was much smaller.

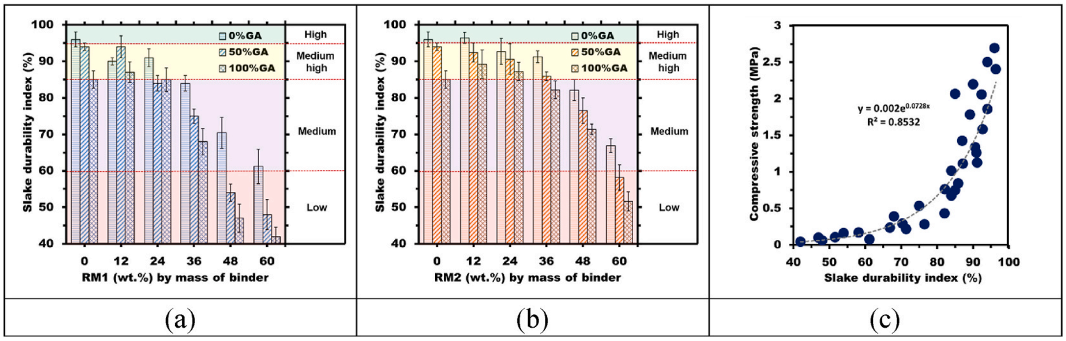

(a) (b) (c)

Fig. 10. Slake durability index (%) of (a) RM1 and (b) RM2 mixtures across the RM (wt.%) by mass of binder and GA (wt.%) by mass of aggregate. (c) Correlation between unconfined compressive strength and slake durability index (%).

3.4. *Mechanical properties*

Fig. 8(a–b) depict the unconfined compressive strength results of all the prepared CLSM specimens. Different from OPC, the hydration of AAMs generates Na and Al incorporated calcium-(sodium) aluminosilicate hydrate (C-(N-)A-S-H) and sodium-aluminosilicate hydrate (N-A-S-H) which function as the major strength-giving and binding materials [18,39]. In this study, the hydration of the ternary blends (i.e., SG, GP and RM) was involved, and the measured strengths were in the range of 0.04 MPa–2.69 MPa, below the upper bound limit for CLSM (i.e., ~8.3 MPa) [1,4]. It should be noted that the strengths were generally much lower than those of many reported AAMs because (i) the specimens were cured at ambient temperature, and (ii) much higher water-to-binder ratios were used to ensure the flowability and self-leveling properties of the CLSM. It was interesting to see the RM-free specimens still yielded the highest compressive strength while the bleeding potential was high (Fig. 6a–b). When RM content is lower than 36 % (by mass of binder), most specimens achieved a strength higher than 0.5 MPa which is the minimum strength required for pedestrian traffic [14]. In terms of the formulations, significant trends are evident: for both RM1 and RM2 mixtures, the compressive strength decreased with increasing percentage of RM and GA. However, the strength was actually more related to the water-to-binder ratio (see Fig. 8c) since a higher water content results in a higher porosity in cementitious materials, thereby impairing the mechanical properties [40]. The addition of RM reduced the flowability, and a considerably more water was required for the CLSM preparation, which might be the major reason for the strength reduction as the RM content increased.

Fig. 9(a–b) show the splitting tensile strength of the CLSM specimens after 28 days of curing, potentially reflecting the CLSM's resistance to cracking, shrinkage and thermal stresses. The results of the mixtures with over 36 % RM by mass of binder were not shown because the measured strengths were too low (~10 KPa) with high uncertainty. It can be seen that the splitting tensile strength ranged from 0.52 MPa to 0.01 MPa, and the trends were similar to those of the compressive strength suggesting a higher RM or GA content always yielded a lower splitting tensile strength. It appears that the use of GA significantly impaired the tensile strength, which could be attributed to a much lower adhesion between glass cullet and the binders [39]. As shown in Fig. 9 (c), a fair linear correlation can be established between the compressive strength and splitting tensile strength (Eq. (4))

$$f_t = 0.2164 \times f_c - 0.1135 \tag{4}$$

Where, f_t: splitting tensile strength (MPa); f_c: unconfined compressive strength (MPa).

3.5. *SDI test*

Fig. 10(a–b) depict the SDI test results of all the CLSM specimens. In general, SDI can assess the susceptibility of a rock- or soil-like material to disintegrate upon exposure to water, and the materials with low SDI values are more susceptible to weathering. The performance after two consecutive cycles of SDI test can be classified as "high" (SDI = 95 %–100 %), "medium-high" (SDI = 85 %–95 %), "medium" (SDI = 60 %–85 %) and "low" (SDI <60 %) [41,42]. As shown in Fig. 8(a–b), the SDI results ranged from 42.1 % to 96.0 %, and the SDI generally decreased with increasing RM and GA contents. When the RM content was low (<~36 % for RM1 mixtures and < ~48 % for RM2 mixtures), the SDI values maintained at high and medium-high levels and were not very sensitive to the components of the CLSM. However, significant reduction in SDI could be observed if the RM content further increased. Fig. 10 (c) shows the correlation between the unconfined compressive strength and SDI results, suggesting the SDI was much more sensitive for the mixtures with lower strength values (<1 MPa). For the higher-strength mixtures (>1 MPa), the SDI values were similar and stayed at higher level. Therefore, the produced CLSM with a very high RM content should be carefully managed and may not be used for the construction of long-term infrastructure.

3.6. *Toxic metal mobility*

The TCLP hazardous waste limit and the US drinking water standard were used to compare with the measured results [43,44]. To

Table 4
Toxic metals present in the leachate of raw materials.

Heavy metals	SG (ppm)	GP (ppm)	RM1 (ppm)	RM2 (ppm)	TCLP hazardous waste limit (ppm)	US drinking water standard (ppm)
As	0.07	<0.01	<0.01	<0.01	5	0.01
Be	<0.01	<0.01	0.08	<0.01	0.1	0.004
Cd	0.02	<0.01	0.05	0.04	1	0.005
Cr	0.14	<0.01	1.74	0.09	5	0.1
Hg	<0.01	<0.01	<0.01	<0.01	0.2	0.002
Ni	0.06	<0.01	0.09	0.14	7	–
Pb	0.18	<0.01	0.74	0.81	5	0.015
Se	<0.01	<0.01	0.02	0.02	1	0.05
Sb	<0.01	<0.01	<0.01	<0.01	1	0.006

Table 5
Toxic metals present in the leachate of RM1 binders.

Heavy metals	0 % RM1	12 % RM1	24 % RM1	36 % RM1	48 % RM1	60 % RM1	TCLP hazardous waste limit (ppm)	US drinking water standard (ppm)
As	<0.01	<0.01	<0.01	<0.01	<0.01	<0.01	5	0.01
Be	<0.01	<0.01	<0.01	<0.01	<0.01	<0.01	0.1	0.004
Cd	<0.01	<0.01	<0.01	<0.01	0.01	0.01	1	0.005
Cr	0.01	0.02	0.16	0.21	0.37	0.45	5	0.1
Hg	<0.01	<0.01	<0.01	<0.01	<0.01	<0.01	0.2	0.002
Ni	<0.01	<0.01	<0.01	<0.01	<0.01	<0.01	7	–
Pb	0.04	0.03	0.07	0.08	0.17	0.16	5	0.015
Se	<0.01	<0.01	<0.01	<0.01	<0.01	<0.01	1	0.05
Sb	<0.01	<0.01	<0.01	<0.01	<0.01	<0.01	1	0.006

Table 6
Toxic metals present in the leachate of RM2 binders.

Heavy metals	0 % RM2	12 % RM2	24 % RM2	36 % RM2	48 % RM2	60 % RM2	TCLP hazardous waste limit (ppm)	US drinking water standard (ppm)
As	<0.01	<0.01	<0.01	<0.01	<0.01	<0.01	5	0.01
Be	<0.01	<0.01	<0.01	<0.01	<0.01	<0.01	0.1	0.004
Cd	<0.01	<0.01	<0.01	<0.01	<0.01	<0.01	1	0.005
Cr	0.01	<0.01	<0.01	<0.01	<0.01	<0.01	5	0.1
Hg	<0.01	<0.01	<0.01	<0.01	<0.01	<0.01	0.2	0.002
Ni	<0.01	<0.01	0.01	<0.01	0.02	0.02	7	–
Pb	0.04	0.05	0.05	0.12	0.17	0.26	5	0.015
Se	<0.01	<0.01	<0.01	<0.01	<0.01	<0.01	1	0.05
Sb	<0.01	<0.01	<0.01	<0.01	<0.01	<0.01	1	0.006

set a baseline, the concentrations of metals leached from the raw materials (i.e., SG, GP, RM1 and RM2) were tested. As shown in Table 4, SG and GP generally had much lower mobile heavy metals than those of RM1 and RM2. Also, RM1 had the highest chromium concentration up to 1.74 ppm, and the second highest concentration was found to be lead (0.74 ppm in RM1 and 0.81 ppm in RM2). The leachates of SG, RM1 and RM2 under the TCLP conditions did not meet the requirements for the US drinking water standard. However, the results suggest the toxic metals of all the raw materials were not readily mobile with the measured concentrations below the TCLP hazardous waste limit (Table 4). The possible explanation is that most of the toxic elements are present in stable crystalline phases as evidenced by the XRD patterns (Fig. 2b).

Tables 5 and 6 summarize the metal concentrations in the leachate of the hardened RM1 and RM2 binders. It can be seen that even smaller concentrations of toxic metals were detected after the alkali-activation of the raw materials. It is expected to be attributed to the immobilization of ions in the hydrated products (i.e., C-(N-)A-S-H, zeolitic phases etc.) [45,46]. Also, the hydration products around the waste material particles might form a diffusion barrier to impede the further dissolution of the grains [47]. Although the standard test method revealed that the CLSM leachate might not cause serious environmental issues, the long-term leaching test under different pH and temperatures and the presence of radionuclides still deserve more investigation.

3.7. Phase assemblages of the reaction products

Fig. 11(a–b) show the XRD diffractograms of the binders in RM1 and RM2 mixtures after the curing for 28 d. Upon alkali-activation, the aluminosilicate raw materials are dissolved, and then the aqueous Ca, Na, Si and Al species will form new hydration products to glue the particles together and enhance the mechanical properties over time [48]. Similar to other reported AAMs, the XRD patterns of the SG-GP-RM-based binders show the C-(N-)A-S-H peak at around 29.5° (2θ) which resembles the poorly crystalline riversideite-type

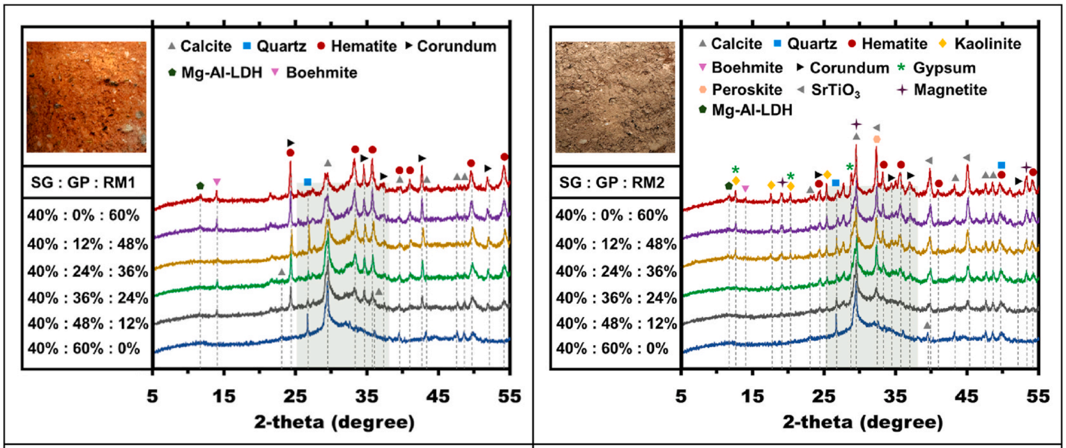

(a) RM1 binders (b) RM2 binders

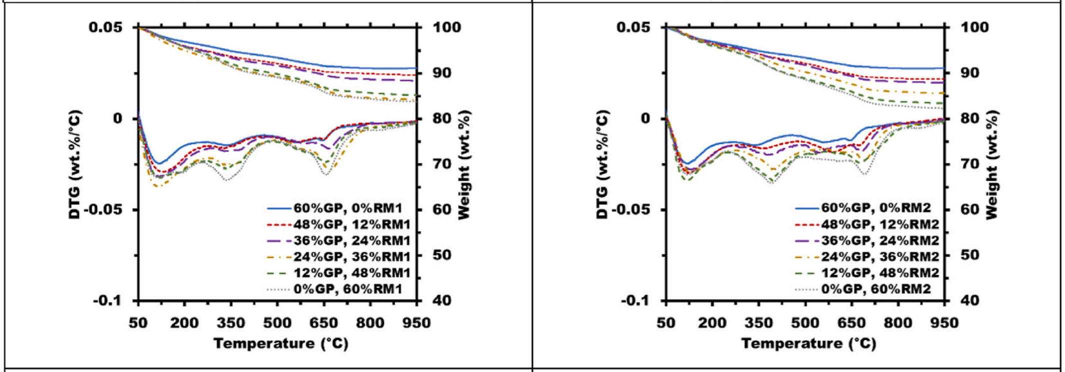

(c) RM1 binders (d) RM2 binders

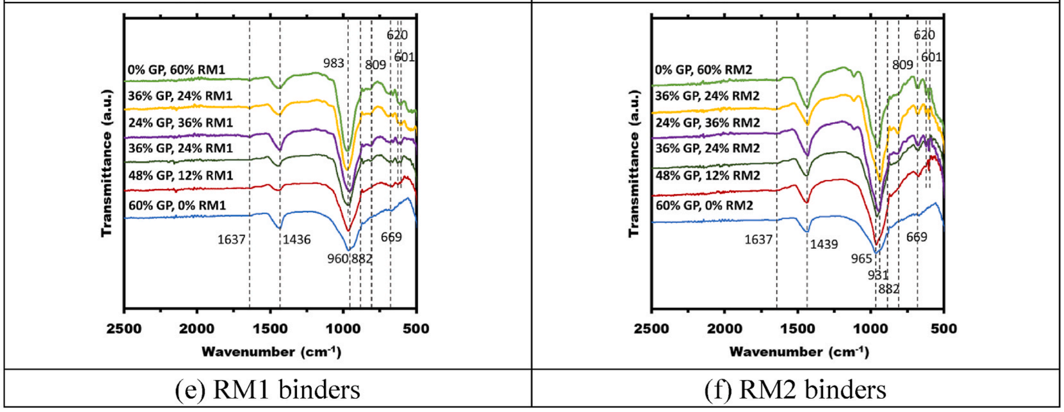

(e) RM1 binders (f) RM2 binders

Fig. 11. XRD, TG and FTIR results of the RM1 and RM2 binders.

C–S–H [29]. These C-(N-)A-S-H peaks generally overlapped with the calcite peaks present in the raw materials (Fig. 2e–f). Mg-Al layered double hydroxide (LDH) as a common secondary hydration product of slag was found at around 11.5° (2θ). Most of the Fe- and Al-rich phases in RM (hematite, magnetite, boehmite etc.) were embedded in the final reaction products in the same crystalline forms probably functioning as the inert fillers in the skeleton.

Fig. 11(c–d) depict the TG results of the binders in this study. Generally, the hydration products in cementitious materials can be distinguished by TG due to the different inherent decomposition temperatures. For the RM-free binders, (C-(N-)A-S-H exhibited degradation in the temperature range of 100–200 °C, and the Mg-Al-LDH phases typically underwent degradation at temperatures ranging from 200 to 450 °C, which is in good agreement with the previous studies [29,49]. The mass drops after 500 °C were associated with the carbonate phases present in the binders [50]. Here the alkali-activated binder based on GP and SG show the similar TG curve in agreement with the previous studies, suggesting the existence of the typical hydration products in AAMs [29,51]. However, by the TG analyses, it appeared to be very challenging to single out the contribution of RM to the hydration processes in the RM-dosed binders

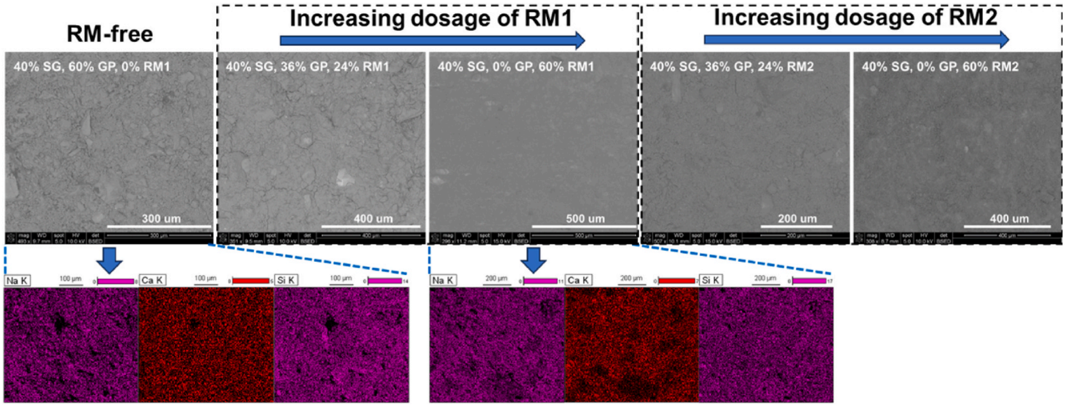

Fig. 12. BSE images of the RM-free, RM1-incorporated (24 % and 60 % RM1) and RM2-incorporated (24 % and 60 % RM2) binders, and the elemental mapping showing the materials are rich in Na, Ca and Si.

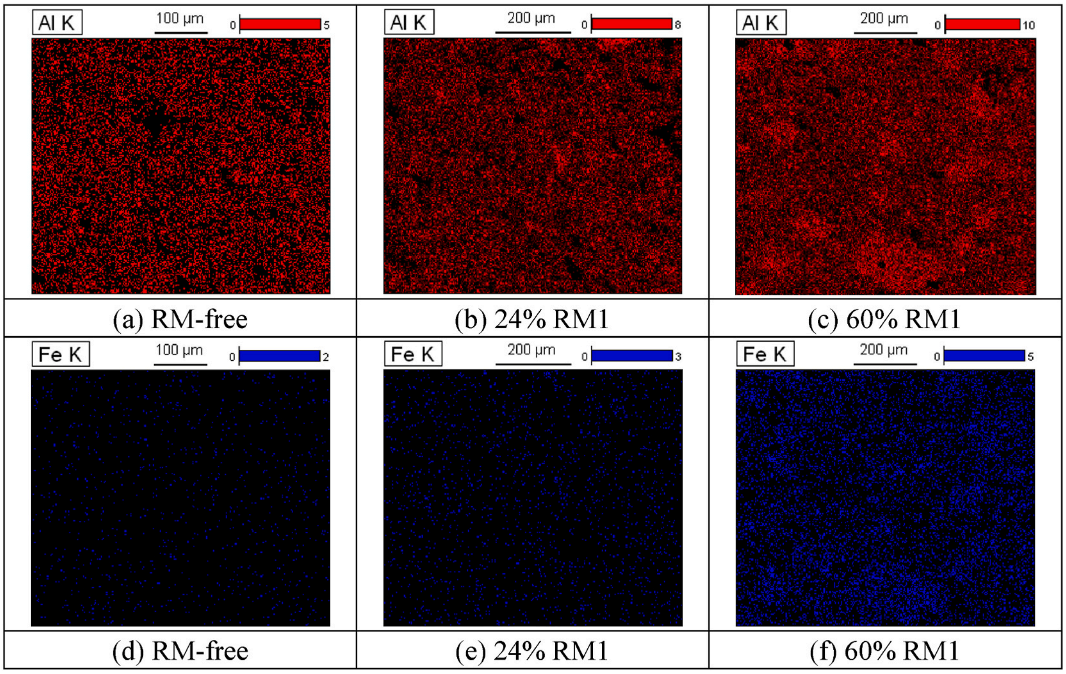

Fig. 13. Elemental mapping showing the distribution of Al and Fe in the RM-free and RM1-incorporated binders with 24 % and 60 % RM1.

considering the significant decomposition of unreacted RM under high temperatures (Fig. 2h). Here only the results of RM2 binders seemed to justify the contribution of RM2 to the formation of C-(N-)A-S-H phases, since the mass loss of the raw RM2 between 50 °C and 200 °C was small while the addition of RM2 slightly increased the amount of C-(N-)A-S-H (Fig. 11d).

Fig. 11(e–f) depict the FTIR spectra of the hardened RM1 and RM2 binders. All the spectra showed the distinct bending vibrations of the T–O–T bonds (T = Si or Al) as the main band at round 983 cm^{-1} – 931 cm^{-1}, suggesting the formation of the typical high-calcium C-(N)-A-S-H phases in AAMs [39,52]. Interestingly, as the RM1 content increased, the T–O–T signals shifted to higher frequencies (960 cm^{-1} to 983 cm^{-1}) while a higher RM2 content tended to lower the band frequency (965 cm^{-1} to 931 cm^{-1}) (Fig. 9e–f). In general, the shift of the main band to a lower frequency indicates the de-polymerisation of SiO_2 network and the incorporation of Al^{3+} ions with the charge balanced by the network modifiers (i.e., Ca^{2+} and Na^{+} etc.). Therefore, the results here might suggest RM2 was more reactive than RM1, providing more Al incorporated into the silica network. The signal at round 809 cm^{-1} was ascribed to the symmetrical stretching vibrations of the O-Si-O bonds [70]. The weak vibration brand located at around 1637 cm^{-1} was attributed to the bending vibrations of hydroxy groups adsorbed on the hydration products AAMs [53]. In addition, the spectra also included the signals corresponding to other secondary phases. For example, the bands located at about 1436 cm^{-1} (RM1 binders) and 1439 cm^{-1} (RM2 binders) correspond to the $\nu_3[CO_3^{2-}]$ while the bands at around 882 cm^{-1} was associated with $\nu_2[CO_3^{2-}]$ and $\nu_4[CO_3^{2-}]$ [39]. The band at around 669 cm^{-1} was ascribed to the stretching vibrations of the Al–O bonds (AlO_4 groups) which was influenced by the Al in RM

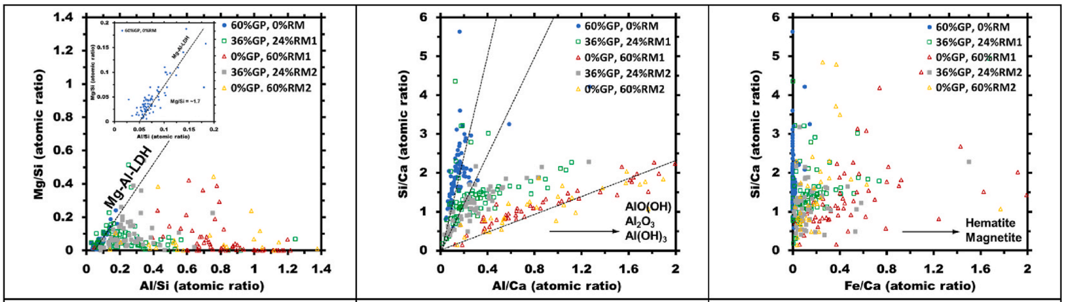

(a) Mg/Si – Al/Si (b) Si/Ca – Al/Ca (c) Si/Ca – Fe/Ca

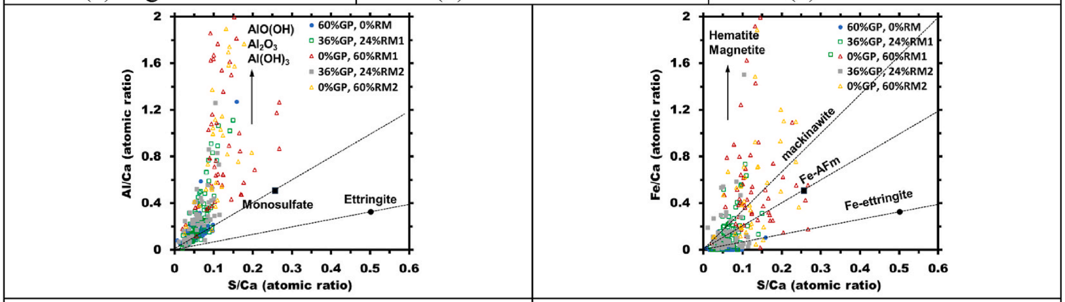

(d) Al/Ca – S/Ca (e) Fe/Ca – S/Ca

Fig. 14. Compositional plots of the phases in the binders with 0 % RM, 24 % RM1, 60 % RM1, 24 % RM2 and 60 % RM2. The BSE-EDS analyses of each specimen involved the acquisition of 60–80 points.

[16]. The Fe-O bonds in hematite and magnetite of the RM were reflected by the narrow bands at around 620 cm^{-1} and 601 cm^{-1} [54].

3.8. BSE-EDS

Fig. 12 shows the BSE images of the RM-free and RM1-and RM2-incorporated (24 % and 60 % RM by mass) binders in this study and the elemental mapping of Na, Ca and Si Fig. 11(a–f) depict the distribution of Al and Fe elements in the matrices as RM1 (or RM2) content increased. The polished specimens embedded in epoxy were utilized in the BSE imaging for the elemental mapping. As shown in Fig. 12, the binding materials, irrespective of the RM incorporation, were generally rich in Na, Ca and Si, reflecting the presence of the C-S-H phases upon NaOH activation. Moreover, Fig. 13 reveals the addition of RM significantly enriched the Al and Fe in the matrices, although the XRD patterns showed that most of the Al and Fe elements stayed in the crystalline phases (Fig. 11a–b). In fact, Al either in major or minor quantities contribute to the formation of AFt and AFm phases and can be incorporated into C-S-H [17,55]. Also, recent studies suggested that Fe was expected to be present in the iron-bearing phases in cementitious materials such as mackinawite, Fe-AFt, Fe-AFm and even amorphous silicate network [56,57].

To further analyze the binders by BSE imaging, compositional plots of the phases were constructed based on the EDS data (Fig. 14a–e). As shown in Fig. 14 (a), the precipitation of hydrotalcite phases (Mg/Al = ~1.7) in the RM-free binder was shown by the dashed line, which agrees with previous studies [29,58]. At the intercept point with Mg/Si = 0, the Al/Si atomic ratio was about 0.05, indicating the approximate Al/Si ratio in the mixed C-(N-)A-S-H and AFm phases. Here the Al/Si ratio was considerably lower than the result (Al/Si = 0.4) reported by Ye et al. [58] probably because the incorporation of GP decreased the total Al content in the binder. Fig. 14(b–c) reveal that as the RM content increased, the bulk Si/Al and Si/Fe decreased due to the presence of more Al and Fe from RM. Also, strong linear relationship could be established in the elemental plot between Si/Ca and Al/Ca, suggesting the replacement of tetrahedral Si^{4+} by Al^{3+} in C-(N-)A-S-H gels, and the imbalance of charge is compensated by the alkali metals available in the system (i.e., Ca, K, Na etc.) [59]. Fig. 14 (c) might suggest the formation of increasing Fe-hydrogarnet as the Fe content increased. Similarly, the Fe-incorporated C-S-H could exit in the products, but the Fe/Si ratio was generally lower than 0.0003 since the pre-precipitation of the other iron-rich phases significantly restricted the Fe uptake in C-S-H [60]. In terms of the Al/Ca versus S/Ca plot, the results showed the adsorption of sulfate on the hydration products (Fig. 14d). It appeared that ettringite was not detected, although the Al content significantly increased with increasing RM. In comparison, the Fe/Ca versus S/Ca plot as shown in Fig. 14 (e) revealed the possible existence of mackinawite, Fe-AFm and Fe-ettringite in the binders. Previous study has shown these Fe-containing phases might exist in the hydration products of AAMs, and mackinawite was even thermodynamically more stable than Fe-AFm and Fe-ettringite in AAMs [56]. However, these phases were not conspicuously shown by the XRD results probably due to the low amount.

3.9. Thermodynamic modeling

Fig. 15(a–d) exhibit the thermodynamic modeling results of four different RM-incorporated mixtures (with 24 % and 60 % RM) in

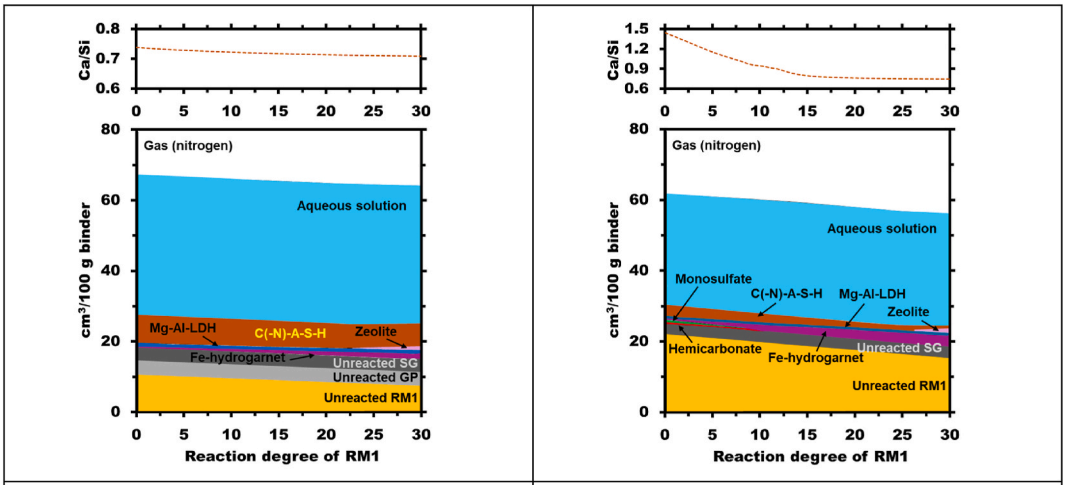

(a) 36% GP and 24% RM1 (b) 0% GP and 60% RM1

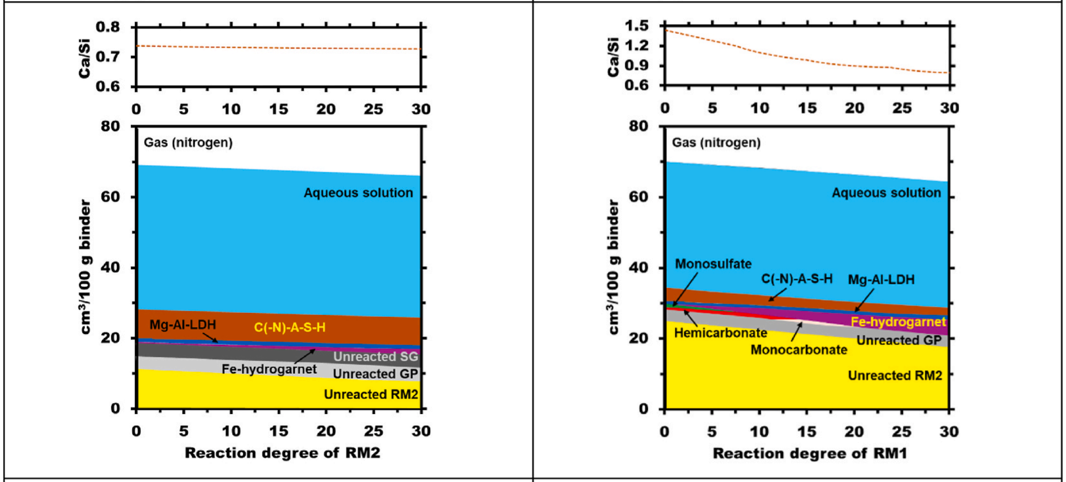

(c) 36% GP and 24% RM2 (d) 0% GP and 60% RM2

Fig. 15. Thermodynamic simulation of four typical RM-incorporated reaction systems and the Ca/Si ratio of the predicted C-(N-)A-S-H assuming different reaction degrees of RM (0 %–30 %). The reactivities of GP and SG were assumed to be 50 %.

Table 7
Unit emission and cost of the raw materials for CLSM.

Materials	Unit emission [a] (kg CO_2/ton)	Unit cost ($/ton)
Cement	830	117.46
Fly ash	9	38.69
Waste glass	–	–
Slag	19	55
Red mud	15	11.08
Solid NaOH	1200	400
Sand	10	46.10
Water	0	2.5

[a] The data were sourced from literatures: Xiao et al. [29]; Yan et al. [68]; Maddalena et al. [69]; Samarakoon et al. [62].

this study across the reactivity of RM. It can be seen that RM1 and RM2 binders showed the similar trends. For example, a higher RM/GP mass ratio results in a less amount of precipitated C-(N-)A-S-H in the system, and more secondary phases (i.e., monosulfate, hemicarbonate and monocarbonate) are predicted at 60 % RM. Therefore, the decreasing strength of the CLSM specimens with increasing RM% could be also on account of the less binding phases in the hydration products (Fig. 8a–b). The hydrotalcite phases (Mg-Al-LDH) are always predicted and governed by the Mg content in SG, which is not influenced by RM. No magnesium aluminosilicate

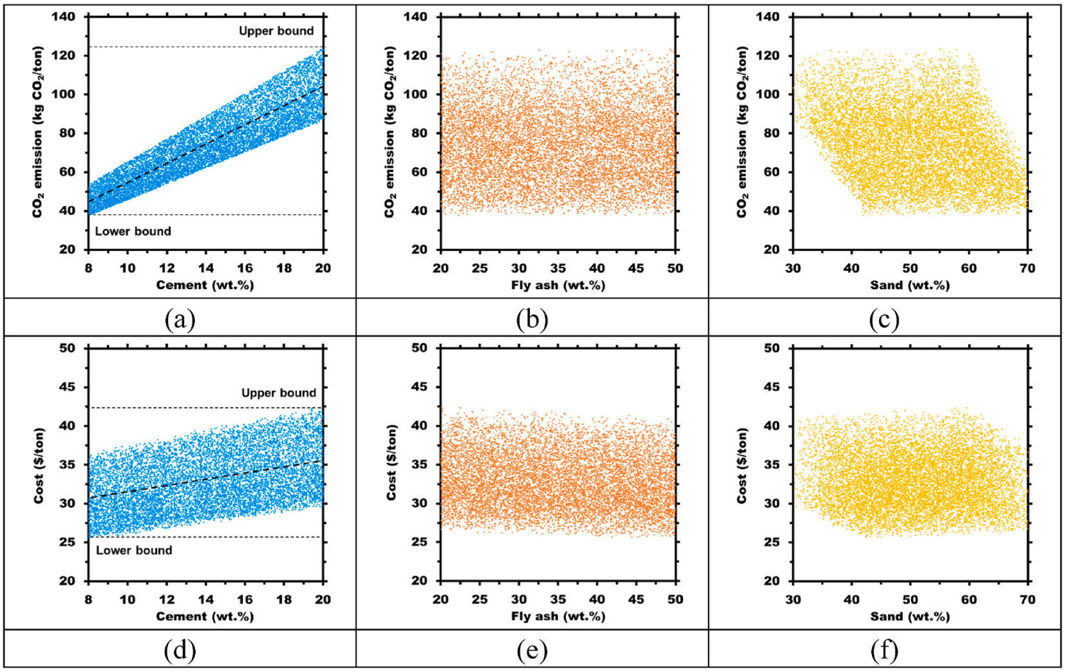

Fig. 16. Monte Carlo simulation-derived CO_2 emission of the traditional CLSM formulations across (a) cement (wt.%), (b) fly ash (wt.%) and (c) sand (wt.%), and the corresponding cost across (d) cement (wt.%), (e) fly ash (wt.%) and (f) sand (wt.%). Ten thousand datasets are included in the simulation.

hydrates (M-A-S-H) are predicted. Based on the simulation, the iron in RM mostly contributed to the formation of Fe-hydrogarnet $(Ca_3(Al_xFe_{1-x})_2(SiO_4)_y(OH)_{4(3-y)})$ as the reactivity of RM increases [61]. However, no mackinawite, Fe-ettringite or Fe-AFm are predicted, and the sulfur content tend to be in aqueous form when the reaction degree of RM is high. In addition, the reaction of RM caused the decalcification of C-(N-)A-S-H (see the decreasing Ca/Si ratio in Fig. 15a–d). Taken together, these results generally reveal SG has more synergistic effect with GP than with RM for the synthesis of AAMs. However, when RM content is not overly high (e.g., 24 % as shown in Fig. 15a–c), the influence of RM on the decalcification of C-(N-)A-S-H is actually negligible.

4. Carbon emission and cost analysis

The basic cost and carbon footprint of the proposed CLSM formulations are compared to those of the traditional CLSM based on OPC, fly ash and natural aggregate. The unit CO_2 emission and the cost of the relevant materials are summarized in Table 7. The crushing process of waste glass is considered to consume electricity at 50 kWh/ton, and the cost and emission for 1 kWh are 0.28 $ and 1.08 kg CO_2 [62]. It is assumed that all the materials are locally available, so the cost and CO_2 emissions associated with transportation are not included here. For the conventional CLSM with OPC and fly ash, Monte Carlo simulation is conducted assuming a wide range of mass ratios for the solid ingredients: 8–20 wt% OPC and 20–50 wt% fly ash [9]. The rest of the solid material is assumed to be natural sand, and a water-to-binder ratio ranging from 0.4 to 1 is considered. An even probability distribution for each input is tentatively used in the modeling.

As shown in Fig. 16(a–f), the lower and upper bounds for the carbon emission and cost were found to be 38.40–123.05 kg CO_2/ton and 25.61–42.29 $/ton, respectively. Also, the CO_2 emission and cost of the traditional CLSM formulations are more sensitive to the OPC content due to the high unit emission and unit cost of cement (Table 6). It can be seen that the average CO_2 emission drastically increases from around 45 kg CO_2/ton to 103 kg CO_2/ton when the cement (wt.%) increases from 8 % to 20 % (Fig. 16a). In comparison, the increase in cost is less significant (Fig. 16d).

Fig. 17(a–d) exhibit the CO_2 emission and cost of the proposed CLSM formulations across the RM and GA contents. As shown in Fig. 17(a–b), the estimated carbon emission data were lower than the average emission of the traditional OPC-based CLSM, highlighting the environmental friendliness of the materials. Also, the new formulations can contribute to the waste management and upcycling of industrial waste. It can be seen that the CO_2 emission decreases with increasing RM content since RM is a ready-to-use waste material while waste glass needs to be crushed. It appears that the cost the RM-incorporated CLSM with virgin aggregate is similar to that of the traditional CLSM, implying the cost of the AAM was close to that of the OPC-fly ash-based binders (Fig. 17c–d). However, the addition of GA remarkably reduces the overall cost, and the mixtures with 100 % GA generally have a lower cost than the estimated minimum cost of the traditional CLSM. Therefore, the use of glass aggregate plays the most important role in controlling the cost of the proposed formulations. Taken together, the results suggest the use of RM and waste glass in CLSM reduce the environmental impacts and cost of the construction, and the proposed CLSM formulations can potentially replace the traditional ones produced by

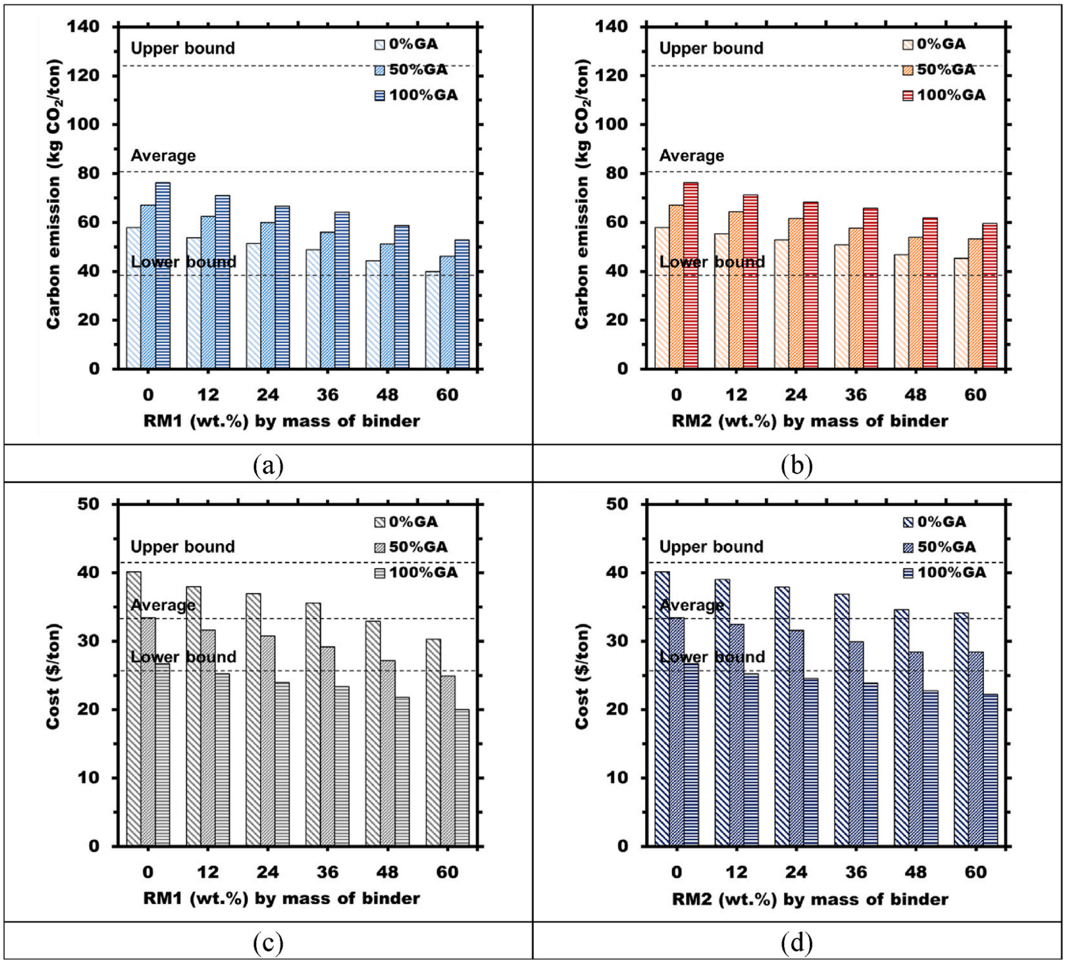

(a) (b)

(c) (d)

Fig. 17. CO_2 emission of the CLSM formulations with (a) RM1 and (b) RM2, and the cost of the CLSM formulations with (c) RM1 and (d) RM2. The upper and lower bounds and the average CO_2 emission (or cost) of the traditional CLSM are shown in each plot.

OPC and fly ash.

5. Conclusions

New alkali-activated CLSM formulations based on urban waste glass and red mud are proposed for the waste upcycling. The reaction mechanism, engineering properties and environmental impacts of the materials were systematically investigated. The outcomes show a wide range of these formulations conform to the typical standards of CLSM and can be potentially utilized for more sustainable construction applications. The main conclusions are summarized as below:

- Waste glass powder exhibited a high content of amorphous silica, whereas red mud contained complex crystalline phases abundant in aluminum and iron, such as boehmite, corundum, and hematite. Additionally, red mud as a ready-to-use waste material had a much finer particle size and clay-like texture, necessitating a higher water demand for the RM-incorporated CLSM to meet the flow consistency requirement.
- Increasing the proportion of red mud to glass powder notably decreased the workability of the CLSM and extended the setting time. Nevertheless, red mud demonstrated high efficacy in enhancing bleeding performance, thereby functioning as a crucial constituent in the suggested formulations.
- The unconfined compressive strength, splitting tensile strength, and slake durability index exhibited a consistent pattern, indicating that a higher content of red mud compromised the mechanical properties. This was attributed in part to the elevated water content necessary to achieve the desired flow consistency.
- Employing glass aggregate typically had negative effects on various engineering properties of the tested CLSM, including reduced flowability, prolonged setting time, increased bleeding potential, and inferior mechanical properties. However, the proper design of CLSM with glass aggregate can still ensure compliance with engineering specifications.

- The standard TCLP test showed the toxic metals in the CLSM were not readily mobile, and the concentrations were below the TCLP hazardous waste limit. After the alkali-activation, even lower concentrations of toxic metals were identified, suggesting the immobilization of the harmful ions in the hydration products.
- The microstructural analyses and thermodynamic modeling revealed the precipitation of C-(N-)A-S-H as the major binding material. The reactive Fe and Al from red mud most probably contributed to the formation of hydrogarnet phases. Slag has more synergistic effect with glass powder than with red mud for the synthesis of AAMs.
- The suggested CLSM formulations typically exhibit reduced CO_2 emissions and lower costs compared to the traditional CLSM produced with OPC and fly ash, highlighting their environmental sustainability and cost-effectiveness.

CRediT authorship contribution statement

Rui Xiao: Writing – review & editing, Writing – original draft, Supervision, Resources, Project administration, Methodology, Investigation, Formal analysis, Conceptualization. **Qingke Nie:** Resources, Project administration, Investigation, Formal analysis. **Xiaodi Dai:** Writing – review & editing, Methodology, Investigation, Formal analysis, Conceptualization. **Zhi Wan:** Investigation, Formal analysis. **Jingtao Zhong:** Investigation, Formal analysis. **Yuetan Ma:** Investigation, Formal analysis. **Baoshan Huang:** Writing – review & editing, Supervision, Resources, Project administration, Funding acquisition, Conceptualization.

Declaration of competing interest

The authors hereby declare NO conflict of interests to the contents of this paper.

Data availability

Data will be made available on request.

References

[1] R. Siddique, Utilization of waste materials and by-products in producing controlled low-strength materials, Resour. Conserv. Recycl. 54 (1) (2009) 1–8.
[2] N.K. Lee, H.K. Kim, I.S. Park, H.K. Lee, Alkali-activated, cementless, controlled low-strength materials (CLSM) utilizing industrial by-products, Construct. Build. Mater. 49 (2013) 738–746.
[3] R. Xiao, P. Polaczyk, X. Jiang, M. Zhang, Y. Wang, B. Huang, Cementless controlled low-strength material (CLSM) based on waste glass powder and hydrated lime: synthesis, characterization and thermodynamic simulation, Construct. Build. Mater. 275 (2021) 122157.
[4] S. Naganathan, H.A. Razak, S.N.A. Hamid, Properties of controlled low-strength material made using industrial waste incineration bottom ash and quarry dust, Mater. Des. 33 (2012) 56–63.
[5] Y.S. Kim, T.M. Do, H.K. Kim, G. Kang, Utilization of excavated soil in coal ash-based controlled low strength material (CLSM), Construct. Build. Mater. 124 (2016) 598–605.
[6] D.A. Ghanad, A.M. Soliman, Bio-based alkali-activated controlled low strength material: engineering properties, Construct. Build. Mater. 279 (2021) 122445.
[7] V. Alizadeh, S. Helwany, A. Ghorbanpoor, K. Sobolev, Design and application of controlled low strength materials as a structural fill, Construct. Build. Mater. 53 (2014) 425–431.
[8] K. Farrag, Controlled low-strength material used around buried pipelines, Transport. Res. Rec. 2251 (1) (2011) 157–164.
[9] S. Bouzalakos, A.W.L. Dudeney, B.K.C. Chan, Formulating and optimising the compressive strength of controlled low-strength materials containing mine tailings by mixture design and response surface methods, Miner. Eng. 53 (2013) 48–56.
[10] S.K. Kaliyavaradhan, T.C. Ling, M.Z. Guo, K.H. Mo, Waste resources recycling in controlled low-strength material (CLSM): a critical review on plastic properties, J. Environ. Manag. 241 (2019) 383–396.
[11] C. Wang, Y. Li, P. Wen, W. Zeng, X. Wang, A comprehensive review on mechanical properties of green controlled low strength materials, Construct. Build. Mater. 363 (2023) 129611.
[12] C.E. Pierce, H. Tripathi, T.W. Brown, Cement kiln dust in controlled low-strength materials, Mater. J. 100 (6) (2003) 455–462.
[13] W.T. Kuo, H.Y. Wang, C.Y. Shu, D.S. Su, Engineering properties of controlled low-strength materials containing waste oyster shells, Construct. Build. Mater. 46 (2013) 128–133.
[14] H. Wu, B. Huang, X. Shu, J. Yin, Utilization of solid wastes/byproducts from paper mills in Controlled Low Strength Material (CLSM), Construct. Build. Mater. 118 (2016) 155–163.
[15] D.M. Roy, Alkali-activated cements opportunities and challenges, Cement Concr. Res. 29 (2) (1999) 249–254.
[16] Y. Wang, R. Xiao, W. Hu, X. Jiang, X. Zhang, B. Huang, Effect of granulated phosphorus slag on physical, mechanical and microstructural characteristics of Class F fly ash based geopolymer, Construct. Build. Mater. 291 (2021) 123287.
[17] R. Xiao, X. Jiang, M. Zhang, P. Polaczyk, B. Huang, Analytical investigation of phase assemblages of alkali-activated materials in CaO-SiO2-Al2O3 systems: the management of reaction products and designing of precursors, Mater. Des. 194 (2020) 108975.
[18] J.L. Provis, Alkali-activated materials, Cement Concr. Res. 114 (2018) 40–48.
[19] R. Xiao, B. Huang, H. Zhou, Y. Ma, X. Jiang, A state-of-the-art review of crushed urban waste glass used in OPC and AAMs (geopolymer): progress and challenges, Cleaner Mater. 4 (2022) 100083.
[20] R. Xiao, Z. Shen, R. Si, P. Polaczyk, Y. Li, H. Zhou, B. Huang, Alkali-activated slag (AAS) and OPC-based composites containing crumb rubber aggregate: physico-mechanical properties, durability and oxidation of rubber upon NaOH treatment, J. Clean. Prod. 367 (2022) 132896.
[21] M.O. Yusuf, M.A.M. Johari, Z.A. Ahmad, M. Maslehuddin, Evolution of alkaline activated ground blast furnace slag–ultrafine palm oil fuel ash based concrete, Mater. Des. 55 (2014) 387–393.
[22] T. Hertel, Y. Pontikes, Geopolymers, inorganic polymers, alkali-activated materials and hybrid binders from bauxite residue (red mud)–Putting things in perspective, J. Clean. Prod. 258 (2020) 120610.
[23] M. Najimi, N. Ghafoori, B. Radke, K. Sierra, M. Sharbaf, Comparative study of alkali-activated natural pozzolan and fly ash mortars, J. Mater. Civ. Eng. 30 (6) (2018) 04018115.
[24] X. Jiang, R. Xiao, M. Zhang, W. Hu, Y. Bai, B. Huang, A laboratory investigation of steel to fly ash-based geopolymer paste bonding behavior after exposure to elevated temperatures, Construct. Build. Mater. 254 (2020) 119267.
[25] R. Xiao, P. Polaczyk, M. Zhang, X. Jiang, Y. Zhang, B. Huang, W. Hu, Evaluation of glass powder-based geopolymer stabilized road bases containing recycled waste glass aggregate, Transport. Res. Rec. 2674 (1) (2020) 22–32.

[26] H. Sutar, S.C. Mishra, S.K. Sahoo, H.S. Maharana, Progress of red mud utilization: an overview, Am. Chem. Sci. J. 4 (3) (2014) 255–279.

[27] T. Noor, A. Javid, A. Hussain, S.M. Bukhari, W. Ali, M. Akmal, S.M. Hussain, Types, sources and management of urban wastes, in: Urban Ecology, Elsevier, 2020, pp. 239–263.

[28] S.D. Wang, X.C. Pu, K.L. Scrivener, P.L. Pratt, Alkali-activated slag cement and concrete: a review of properties and problems, Adv. Cement Res. 7 (27) (1995) 93–102.

[29] R. Xiao, Y. Zhang, X. Jiang, P. Polaczyk, Y. Ma, B. Huang, Alkali-activated slag supplemented with waste glass powder: laboratory characterization, thermodynamic modelling and sustainability analysis, J. Clean. Prod. 286 (2021) 125554.

[30] I. You, S. Seo, M. Kim, S.J. Lee, N. Lee, Y. Lee, D.Y. Yoo, ASR potential of alkali-activated soda-lime glass powder in the absence of calcium sources, Cement Concr. Compos. 139 (2023) 105027.

[31] R. Xiao, X. Jiang, Y. Wang, Q. He, B. Huang, Experimental and thermodynamic study of alkali-activated waste glass and calcium sulfoaluminate cement blends: shrinkage, efflorescence potential, and phase assemblages, J. Mater. Civ. Eng. 33 (11) (2021) 04021312.

[32] M. Refaat, A. Mohsen, E.S.A. Nasr, M. Kohail, Minimizing energy consumption to produce safe one-part alkali-activated materials, J. Clean. Prod. 323 (2021) 129137.

[33] P. Wang, D.Y. Liu, Physical and chemical properties of sintering red mud and bayer red mud and the implications for beneficial utilization, Materials 5 (10) (2012) 1800–1810.

[34] B. Lothenbach, D.A. Kulik, T. Matschei, M. Balonis, L. Baquerizo, B. Dilnesa, G.D. Miron, R.J. Myers, Cemdata18: a chemical thermodynamic database for hydrated Portland cements and alkali-activated materials, Cement Concr. Res. 115 (2019) 472–506.

[35] K. Afshinnia, P.R. Rangaraju, Impact of combined use of ground glass powder and crushed glass aggregate on selected properties of Portland cement concrete, Construct. Build. Mater. 117 (2016) 263–272.

[36] S. de Castro, J. de Brito, Evaluation of the durability of concrete made with crushed glass aggregates, J. Clean. Prod. 41 (2013) 7–14.

[37] A. Hajimohammadi, J.L. Provis, J.S. Van Deventer, Time-resolved and spatially-resolved infrared spectroscopic observation of seeded nucleation controlling geopolymer gel formation, J. Colloid Interface Sci. 357 (2) (2011) 384–392.

[38] X. Chen, A. Sutrisno, L.J. Struble, Effects of calcium on setting mechanism of metakaolin-based geopolymer, J. Am. Ceram. Soc. 101 (2) (2018) 957–968.

[39] R. Xiao, X. Dai, J. Zhong, Y. Ma, X. Jiang, J. He, Y. Wang, B. Huang, Toward waste glass upcycling: preparation and characterization of high-volume waste glass geopolymer composites, Sustain. Mater. Technolo. 40 (2024) e00890.

[40] C. Ng, U.J. Alengaram, L.S. Wong, K.H. Mo, M.Z. Jumaat, S. Ramesh, A review on microstructural study and compressive strength of geopolymer mortar, paste and concrete, Construct. Build. Mater. 186 (2018) 550–576.

[41] T. Ersöz, T. Topal, Classification and modification of slake durability test for different types of rocks, Bull. Eng. Geol. Environ. 83 (4) (2024) 139.

[42] T.P. Gautam, A. Shakoor, A durability classification of clay-bearing rocks based on particle size distribution of slaked material, Environ. Eng. Geosci. 23 (2) (2017) 125–136.

[43] J.D. Lincoln, O.A. Ogunseitan, A.A. Shapiro, J.D.M. Saphores, Leaching assessments of hazardous materials in cellular telephones, Environ. Sci. Technol. 41 (7) (2007) 2572–2578.

[44] V. Intrakamhaeng, K.A. Clavier, T.G. Townsend, Hazardous waste characterization implications of updating the toxicity characteristic list, J. Hazard Mater. 383 (2020) 121171.

[45] M.M. Alonso, A. Pasko, C. Gascó, J.A. Suarez, O. Kovalchuk, P. Krivenko, F. Puertas, Radioactivity and Pb and Ni immobilization in SCM-bearing alkali-activated matrices, Construct. Build. Mater. 159 (2018) 745–754.

[46] S. Lee, A. Van Riessen, C.M. Chon, N.H. Kang, H.T. Jou, Y.J. Kim, Impact of activator type on the immobilisation of lead in fly ash-based geopolymer, J. Hazard Mater. 305 (2016) 59–66.

[47] J.G. Jang, S.M. Park, H.K. Lee, Physical barrier effect of geopolymeric waste form on diffusivity of cesium and strontium, J. Hazard Mater. 318 (2016) 339–346.

[48] A. Fernández-Jiménez, N. Cristelo, T. Miranda, Á. Palomo, Sustainable alkali activated materials: precursor and activator derived from industrial wastes, J. Clean. Prod. 162 (2017) 1200–1209.

[49] E. Adesanya, K. Ohenoja, A. Di Maria, P. Kinnunen, M. Illikainen, Alternative alkali-activator from steel-making waste for one-part alkali-activated slag, J. Clean. Prod. 274 (2020) 123020.

[50] J. Wang, X. Lyu, L. Wang, X. Cao, Q. Liu, H. Zang, Influence of the combination of calcium oxide and sodium carbonate on the hydration reactivity of alkali-activated slag binders, J. Clean. Prod. 171 (2018) 622–629.

[51] M. Palacios, F. Puertas, Effect of carbonation on alkali-activated slag paste, J. Am. Ceram. Soc. 89 (10) (2006) 3211–3221.

[52] M. Torres-Carrasco, F. Puertas, Waste glass as a precursor in alkaline activation: chemical process and hydration products, Construct. Build. Mater. 139 (2017) 342–354.

[53] M.O. Yusuf, Bond characterization in cementitious material binders using Fourier-transform infrared spectroscopy, Appl. Sci. 13 (5) (2023) 3353.

[54] A. Radoń, M. Kądziołka-Gaweł, D. Łukowiec, P. Gębara, K. Cesarz-Andraczke, A. Kolano-Burian, P. Włodarczyk, M. Polak, R. Babilas, Influence of magnetite nanoparticles shape and spontaneous surface oxidation on the electron transport mechanism, Materials 14 (18) (2021) 5241.

[55] G.K. Sun, J.F. Young, R.J. Kirkpatrick, The role of Al in C–S–H: NMR, XRD, and compositional results for precipitated samples, Cement Concr. Res. 36 (1) (2006) 18–29.

[56] B. Lothenbach, A. Gruskovnjak, Hydration of alkali-activated slag: thermodynamic modelling, Adv. Cement Res. 19 (2) (2007) 81–92.

[57] A. Baral, C. Pesce, Z. Zhakiyeva, R. Snellings, T. Hanein, J.L. Provis, A. Peys, Characterisation of iron-rich cementitious materials, Cement Concr. Res. 177 (2024) 107419.

[58] H. Ye, Z. Chen, L. Huang, Mechanism of sulfate attack on alkali-activated slag: the role of activator composition, Cement Concr. Res. 125 (2019) 105868.

[59] I.G. Richardson, The calcium silicate hydrates, Cement Concr. Res. 38 (2) (2008) 137–158.

[60] J. Siramanont, B.J. Walder, L. Emsley, P. Bowen, Iron incorporation in synthetic precipitated calcium silicate hydrates, Cement Concr. Res. 142 (2021) 106365.

[61] B.Z. Dilnesa, B. Lothenbach, G. Renaudin, A. Wichser, D. Kulik, Synthesis and characterization of hydrogarnet Ca3 (AlxFe1−x) 2 (SiO4) y (OH) 4 (3−y), Cement Concrete Res. 59 (2014) 96–111.

[62] M.H. Samarakoon, P.G. Ranjith, W.H. Duan, V.R.S. De Silva, Properties of one-part fly ash/slag-based binders activated by thermally-treated waste glass/NaOH blends: a comparative study, Cement Concr. Compos. 112 (2020) 103679.

[63] A.A. Shakir, S. Naganathan, K.N. Mustapha, Properties of bricks made using fly ash, quarry dust and billet scale, Construct. Build. Mater. 41 (2013) 131–138.

[64] M. Ibrahim, M.K. Rahman, S.K. Najamuddin, Z.S. Alhelal, C.E. Acero, A review on utilization of industrial by-products in the production of controlled low strength materials and factors influencing the properties, Construct. Build. Mater. 325 (2022) 126704.

[65] D. Trejo, K.J. Folliard, L. Du, Sustainable development using controlled low-strength material, in: Proceedings of International Workshop on Sustainable Development and Concrete Technology, 2004, May, pp. 231–250.

[66] N. Latifi, A. Eisazadeh, A. Marto, C.L. Meehan, Tropical residual soil stabilization: a powder form material for increasing soil strength, Construct. Build. Mater. 147 (2017) 827–836.

[67] S.K. Parhi, S. Dwibedy, S. Panda, S.K. Panigrahi, A comprehensive study on controlled low strength material, J. Build. Eng. (2023) 107086.

[68] P. Yan, B. Chen, M.A. Haque, T. Liu, Influence of red mud on the engineering and microstructural properties of sustainable ultra-high performance concrete, Construct. Build. Mater. 396 (2023) 132404.

[69] R. Maddalena, J.J. Roberts, A. Hamilton, Can Portland cement be replaced by low-carbon alternative materials? A study on the thermal properties and carbon emissions of innovative cements, J. Clean. Prod. 186 (2018) 933–942.

[70] S.M. Abo-Naf, F.H. El Batal, M.A. Azooz, Characterization of some glasses in the system SiO2, Na2O· RO by infrared spectroscopy, Mater. Chem. Phys. 77 (3) (2003) 846–852.